

Rising from the Ashes II: Did the Birth of the Milky Way's Bar Give Birth to the Birth of the Abundance Bimodality

1 ANGUS BEANE,¹ JAMES W. JOHNSON,² AND ET AL

2 ¹*Center for Astrophysics | Harvard & Smithsonian, Cambridge, MA, USA*

3 ²*The Observatories of the Carnegie Institution for Science, Pasadena, CA, USA*

ABSTRACT

5 The Milky Way is known to host at least two modes in its present day distribution of Fe and α -elements. The
6 exact cause of this bimodality is disputed, but one class of explanations involves the merger between the Milky
7 Way and a relatively massive satellite (Gaia-Sausage-Enceladus) at $z \sim 2$. However, reproducing this bimodality
8 in simulations is not straightforward, with conflicting results on the prevalence, morphology, and mechanism
9 behind multimodality. We present a case study of a galaxy in the Illustris TNG50 simulation which undergoes a
10 sequence of starburst, brief quiescence, and then rejuvenation. After a minor post-processing step which boosts
11 the $[\alpha/\text{Fe}]$ of old star particles, we demonstrate that this galaxy hosts a strongly bimodal distribution in the
12 $[\alpha/\text{Fe}]\text{-}[\text{Fe}/\text{H}]$ plane. The high- and low- α sequences are neatly separated in time by the brief quiescent period.
13 The quiescent period in this galaxy is not associated with a merger but by the formation of a bar followed by AGN
14 activity. This galaxy indicates a novel scenario in which the α -bimodality is caused by AGN-induced quenching
15 triggered by the formation of the Milky Way's bar. We argue that the post-processing step can be interpreted as
16 the TNG model underproducing star formation in the densest regions at high- z .

17 **Keywords:** Classical Novae (251) — Ultraviolet astronomy(1736) — History of astronomy(1868) — Interdis-
18 ciplinary astronomy(804)

1. INTRODUCTION

20 The stellar surface abundances of most elements retain
21 the composition of their natal gas cloud. Therefore, the
22 present-day distribution of stellar surface abundances encodes
23 the chemical history of a galaxy's gas phase. Two elements have received particular interest in the Milky Way: Fe and α -elements (elements produced through the α -process, such as O and Mg). Fe is produced in both Type Ia and Type II SNe whereas α -elements are produced predominantly through Type II SNe. Because these SNe occur on different timescales (10s of Myr after star formation for Type II, as compared to 100s of Myr to Gyrs for Type Ia), the ratio between α -elements and Fe is expected to generally decrease with time.

33 Because of their separate formation channels, the two dimensional plane of $[\alpha/\text{Fe}]\text{-}[\text{Fe}/\text{H}]$ has received considerable interest. In the Milky Way, there is a well-established bimodality with separate high- and low- α sequences (Gratton et al. 1996; Fuhrmann 1998, 2004; Reddy et al. 2006; Adibekyan et al. 2011, 2012; Bensby et al. 2014; Nidever et al. 2014; Hayden et al. 2020). This bimodal distribution is shown in the upper left panel of Figure 1.

41 There are essentially two approaches to explaining the bimodality. First, it is a result of internal secular processes that generate the bimodality through radial migration (Schönrich

44 & Binney 2009; Sharma et al. 2021; Chen et al. 2023) or clump formation (Clarke et al. 2019; Beraldo e Silva et al. 2020, 2021; Garver et al. 2023).

47 Second, the bimodality is generated through gas infall scenarios, either from specific gas accretion episodes from the intergalactic medium (Chiappini et al. 1997; Chiappini 2009; Grisoni et al. 2017; Spitoni et al. 2019), or through a more self-consistent collapse sequence of the circumgalactic medium driven through feedback (Khoperskov et al. 2021). Third and finally, the bimodality is generated through a merger process, either by enhancing the SFR of the Galaxy (Brook et al. 2004, 2005, 2007; Richard et al. 2010) or by supplying a relatively pristine gas supply that resets the metallicity of the Galaxy (Buck 2020; Ciucă et al. 2024). The fact that the Milky Way did undergo a merger with the Gaia-Sausage-Enceladus (GSE) satellite supports these scenarios (Belokurov et al. 2018; Helmi et al. 2018; Naidu et al. 2020; Chandra et al. 2024).

62 In Beane (2024) we argued for an alternate formation scenario of the bimodality, for which we provide further support in this work. In this scenario, the bimodality is formed through a brief quiescent period in the Galaxy's history. During this period, which lasted ~ 300 Myr in that setup, two things happen. First, as the chemical evolution of the galaxy proceeds, fewer stars form. Second, because the SFR is lower,

⁶⁹ α -element production drops and so the $[\alpha/\text{Fe}]$ of the gas
⁷⁰ drops as well. This is conceptually similar to some variants
⁷¹ of the two-phase infall scenarios which allow for a brief halt
⁷² in the star formation rate (Spitoni et al. 2024, and references
⁷³ therein), though the quiescent period is much shorter in Beane
⁷⁴ (2024). The combination of these two effects is what leads to
⁷⁵ the valley in between the high- and low- α sequences.

⁷⁶ In that work, we used idealized simulations of a galaxy
⁷⁷ merger that triggered a starburst which preceded the quies-
⁷⁸ cent period. However, we argued that the merger aspect of
⁷⁹ that work was not necessary, but rather the quiescence. In this
⁸⁰ work, we study a subhalo from the Illustris TNG50 simulation
⁸¹ which demonstrates this. This subhalo of interest (SoI) ex-
⁸² hibits the sequence of events presented in Beane (2024) after
⁸³ a simple post-processing step which enhances the $[\alpha/\text{Fe}]$ of
⁸⁴ old star particles. The SoI undergoes a brief quiescent period
⁸⁵ which neatly separates a high- and low- α sequence. How-
⁸⁶ ever, instead of being preceded by a merger, the quenching is
⁸⁷ preceded by apparent bar-induced AGN activity. Therefore,
⁸⁸ this work serves as a verification that the scenario in Beane
⁸⁹ (2024) is possible in cosmological simulations and can occur
⁹⁰ in non-merger scenarios.

⁹¹ In Section 2 we discuss our selection technique which led to
⁹² discovering the SoI, the observations we use for comparison,
⁹³ as well as a simple one zone chemical evolution model we use
⁹⁴ to justify our post-processing step. In Section 3 we present the
⁹⁵ main results which we discuss and interpret in Section 4. We
⁹⁶ conclude in Section 5.

2. METHODS

2.1. *IllustrisTNG Sample*

⁹⁹ We have made use of the Illustris TNG50 simulation
¹⁰⁰ (Pillepich et al. 2019; Nelson et al. 2019), a cosmological
¹⁰¹ simulation of a ~ 50 cMpc box at high resolution ($m_{\text{baryon}} \sim$
¹⁰² $8.5 \times 10^4 M_{\odot}$). It uses the gravito-magneto-hydrodynamics
¹⁰³ code AREPO (Springel 2010; Pakmor et al. 2016), along with
¹⁰⁴ the TNG model (Vogelsberger et al. 2013; Weinberger et al.
¹⁰⁵ 2017; Pillepich et al. 2018). This model includes several sub-
¹⁰⁶ grid processes: a wind generation model, chemical enrich-
¹⁰⁷ ment from supernovae and asymptotic giant branch stars, and
¹⁰⁸ thermal and kinetic feedback from AGN.

¹⁰⁹ One piece of the TNG model of note for this work is
¹¹⁰ the BH accretion and feedback method (Weinberger et al.
¹¹¹ 2017). The black hole accretion rate (\dot{M}_{BH}) is computed us-
¹¹² ing the local structure of the gas phase with the Bondi-Hoyle-
¹¹³ Lyttleton formula (Hoyle & Lyttleton 1939; Bondi & Hoyle
¹¹⁴ 1944; Bondi 1952), with a maximum of the Eddington accre-
¹¹⁵ tion rate (\dot{M}_{edd}). The model allows the BH to be either in a
¹¹⁶ kinetic radio-mode or a thermal quasar-mode. If the Edding-
¹¹⁷ ton ratio ($\dot{M}_{\text{BH}}/\dot{M}_{\text{edd}}$) exceeds a threshold (M_{BH} -dependent,
¹¹⁸ but $\sim 0.001 - 0.1$), the BH is in the quasar mode and injects
¹¹⁹ a large amount of thermal energy into its surroundings.

¹²⁰ Using the public catalog, we selected a sample of subhalos
¹²¹ at $z = 1.5$ (snapshot 40) according to the following crite-
¹²² ria: (1) the subhalo is central (i.e., the most massive subhalo
¹²³ within its halo), and (2) the subhalo's stellar mass is between
¹²⁴ 10^{10} and $10^{10.5} M_{\odot}/\text{h}$. There were a total of 168 subhalos that
¹²⁵ met both criteria. The chosen mass range is broadly consis-
¹²⁶ tent with the expected mass of the Milky Way at this redshift
¹²⁷ (van Dokkum et al. 2013). We chose to make our selection
¹²⁸ of galaxies at $z = 1.5$ instead of at lower redshift because we
¹²⁹ wished to capture the *formation* of any multimodal structure.
¹³⁰ We did not want contamination by mergers at lower redshift
¹³¹ which we know contribute very little to the Milky Way's disk
¹³² stars (e.g., Bland-Hawthorn & Gerhard 2016).

¹³³ We examined the abundance distribution in the $[\text{Mg}/\text{Fe}]$ -
¹³⁴ $[\text{Fe}/\text{H}]$ plane of this sample of subhalos by eye. Not many
¹³⁵ subhalos had multimodal structure, and any structure that
¹³⁶ was present was relatively weak compared to that observed
¹³⁷ in the Milky Way. We then applied a post-processing to the
¹³⁸ $[\text{Mg}/\text{Fe}]$ of stars by adding to each star particle a value of
¹³⁹ $0.1 \times (t_{1.5} - t_{\text{form}})$, where $t_{1.5}$ is the age of the universe at
¹⁴⁰ $z = 1.5$ (~ 4.3 Gyr) and t_{form} is the formation time of each
¹⁴¹ star particle. With this post-processing, we found that much
¹⁴² more structure was generally present.

¹⁴³ We show the abundance distributions (replicating Figure 1)
¹⁴⁴ of 16 random subhalos from our catalog, and the subhalo we
¹⁴⁵ selected, in Appendix B. Of these subhalos, some structure
¹⁴⁶ is present, but none have a strong bimodality as seen in the
¹⁴⁷ Milky Way. After the α -enhancement, a few have strongly
¹⁴⁸ bimodal features (subject to interpretation): 172175, 178140,
¹⁴⁹ 193025.

¹⁵⁰ We selected subhalo 172175 (the ID at snapshot 40) for its
¹⁵¹ particular resemblance to the Milky Way. We then studied
¹⁵² the main descendant of this subhalo at $z = 0$ (subhalo 392276
¹⁵³ at snapshot 99). We refer to this subhalo as our subhalo of
¹⁵⁴ interest (SoI).

2.2. *Bar Catalog*

¹⁵⁵ In order to study the evolution of the morphology of our
¹⁵⁶ SoI, we make use of the Zana et al. (2022) catalog. They pro-
¹⁵⁷ vide a decomposition of all galaxies with at least 10^4 star par-
¹⁵⁸ ticles, as well as an estimate of the bar strength. This taken to
¹⁵⁹ be the maximum of the second Fourier mode ($A_{2,\text{max}}$) within
¹⁶⁰ the bar region (not including spiral arms).

2.3. *Observations*

¹⁶¹ We make use of two observational data sets. First, we
¹⁶² use the ASPCAP DR17 catalog of stellar abundances (García
¹⁶³ Pérez et al. 2016, J.A. Holtzman et al., in preparation). We
¹⁶⁴ make the same selection cuts as in Beane (2024), described in
¹⁶⁵ their Section 2.4. These are meant to select only giants with
¹⁶⁶ high quality abundance measurements as well as restricting
¹⁶⁷ the sample to only stars in the disk with angular momenta

similar to the Sun's. This results in a sample of 54,777 stars. We use Fe to track total metallicity and Mg alone as an α -element.

We then further considered a dataset of stellar ages from the APOKASC2 catalog (Pinsonneault et al. 2018). This uses a combination of APOGEE spectroscopic parameters and *Kepler* time series photometry to compute astroseismic ages. Using only stars with 25% age uncertainties (taken as the maximum of the upper and lower uncertainty), we cross-match this catalog to our larger sample from ASPCAP which results in a sample of 1201 stars.

2.4. One-Zone Chemical Evolution Model

James inserts his section

3. RESULTS

3.1. Abundance Plane

The main result of our paper is given in Figure 1. Here, we compare the abundance plane in the Milky Way (left column) to that in our subhalo of interest (middle and right columns). The upper panels show the 2D distribution in the space of [Mg/Fe]-[Fe/H]. We have applied the standard `scipy` implementation of a gaussian kernel density estimator to a Cartesian grid of points. For each panel, we normalize so that the integral of the distribution is unity. Colors are plotted in a log scale ranging from 0.08 to 15 dex⁻². Contour lines are plotted at 0.1, 1.5, and 10 dex⁻².

The colored vertical lines are indicated at [Fe/H] = -0.75, -0.5, -0.25, and 0 dex in the Milky Way, and at bins 0.25 dex higher in the simulations. The lower panels show 1D histograms of [Mg/Fe] in bins centered on these values. The bins for the Milky Way/simulations have width 0.2/0.05 dex. The [Mg/Fe] values are given offsets so their medians are at zero. The rationale for the higher plotted [Fe/H] in the simulations comes just from the empirical location of the bimodalities. The Milky Way shows a clear bimodal population, with a high- α sequence most clearly distinct from the low- α sequence at low metallicity. The two sequences merge around solar metallicity.

Our SoI, on the other hand, does not show a clearly bimodal structure in the fiducial simulation (middle column). There is some structure in the [Fe/H] = -0.75 bin. The right panel of Figure 1 shows the same distribution as in the middle panel, but with a post-processed declination in [Mg/Fe] described in Section 2.1. Star particles formed before $z = 1.5$ are given an additive offset of $0.1 \times (t_{1.5} - t_{\text{form}})$, where $t_{1.5}$ is the age of the universe at $z = 1.5$ and t_{form} is the formation time of the star particle. A multimodal structure emerges with three clear modes at [Mg/Fe] $\sim 0.8, 0.5$, and 0.2 dex. The 1D histograms show that the modes are well-separated, and that the troughs between the modes nearly vanish.

3.2. Alpha Time Dependence

The abundance distributions shown in Figure 1 can be better understood by examining the evolution of [Mg/Fe] with time of the individual stars/star particles. In the upper panels of Figure 2 we show the true distribution of [Mg/Fe] as a function of time for the fiducial SoI in the middle and for the post-processed, α -enhanced subhalo to the right. We use age instead of formation time in order to better facilitate comparisons to observations. These panels are true 2D histograms, with a logarithmic colormap normalized to the maximum of the plot. The values of [Mg/Fe] are offset so their medians are at zero.

There is a gap in the ages that occurs at an age of 10.6 Gyr, which we mark with a vertical dashed line. Star particles older than this line have a much clearer gradient in time with [Mg/Fe] than stars that form after. In the [Fe/H] = -0.25 bin, star particles which form directly after this line have a slightly depressed [Mg/Fe] than stars which form a short time later.

In the lower panels we plot to the left data from the Milky Way and to the middle and right from the fiducial and α -enhanced SoI, respectively. For the simulations, we add 15% age and 0.01 dex [Mg/Fe] Gaussian errors. These values are roughly in line with the observational errors from the APOKASC2 and APOGEE datasets that the lower left panel is made from (see Appendix A for plots of the observational errors). The error in [Mg/Fe] is not significant, but the age error, which is 1.5 Gyr at 10 Gyr, smears out the distribution before and after the dashed line. The α -enhanced SoI still shows two separate populations in this plot, but they now significantly overlap in age.

The Milky Way distribution (lower left panel) bears some resemblance to the α -enhanced SoI. In particular, the [Fe/H] = -0.5 and -0.25 bins (blue and orange, respectively) show what appears to be two populations overlapping in age but nonetheless separated in [Mg/Fe]. These are the bins at which the bimodality is strongest (upper left panel of Figure 1).

3.3. Evolutionary History

In an effort towards understanding the events in our SoI's history that led to the behavior around the dashed line in Figure 2, we examine the evolution of some of its key quantities. In the upper panel of Figure 3, we show the SFH of our galaxy with the same dashed line as in Figure 2 (at an age of 10.6 Gyr in that plot is at a time of ~ 3.2 Gyr here). This SFH is computed using the SFR within twice the stellar half-mass radius in our SoI's main progenitors. We see two peaks in the SFH at $t \sim 2.5$ and ~ 4.5 Gyr of an amplitude of about 50 and $30 M_\odot/\text{yr}$. The dashed line corresponds to a relative drop in the SFR, down to about $3 M_\odot/\text{yr}$ before quickly recovering.

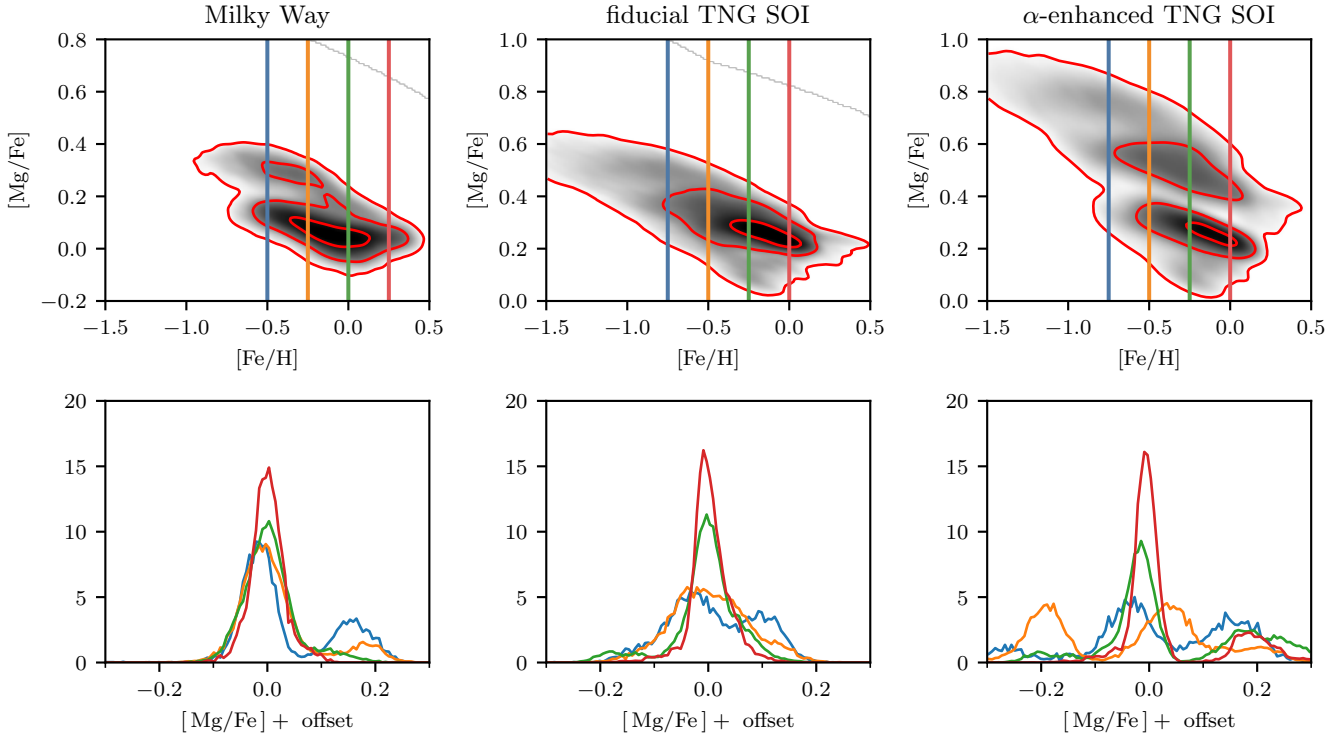


Figure 1. When old stars are α -enhanced, our subhalo of interest from TNG displays a prominent bimodality. The upper left panel shows the distribution in the $[\text{Mg}/\text{Fe}]$ - $[\text{Fe}/\text{H}]$ plane of the Milky Way, demonstrating a clear bimodality (data selection given in text). The lower left panel shows the 1D histograms of $[\text{Mg}/\text{Fe}]$ at fixed $[\text{Fe}/\text{H}]$ values of -0.5 , -0.25 , 0 , and 0.25 (blue, orange, green, and red, respectively). In the Milky Way, the bimodality is strongest at low metallicities while disappearing at high metallicities. The middle column shows the same plots but for our TNG subhalo of interest (392276) and with the fixed $[\text{Fe}/\text{H}]$ values 0.25 dex lower. Only faint structure is seen in the lowest bin (blue, -0.75 dex). The right column shows the same subhalo but after increasing the $[\text{Mg}/\text{Fe}]$ value of star particles formed before $z = 1.5$ linearly with formation time (specifically by incrementing $[\text{Mg}/\text{Fe}]$ by $0.1 \times (t_{1.5} - t_{\text{form}})$ if $t_{\text{form}} < t_{1.5}$, where $t_{1.5}$ is the age of the universe at $z = 1.5$). A clear bimodality is shown in these panels which, unlike in the Milky Way, is present at all metallicities.

269 The middle panel shows the accretion rate of the central
270 black hole as a fraction of the maximum (Eddington) accre-
271 tion rate. Early in its history ($t < 2$ Gyr), the subhalo ex-
272 periences high accretion rates. The accretion rate then steadily
273 declines until $t \sim 5$ Gyr at which point it fails to show on this
274 linear plot. However, at the dashed line (~ 3.2 Gyr) there is a
275 localized peak in the accretion rate, maxing out at about 30%
276 Eddington. This places the BH firmly in the thermal quasar-
277 mode, and allows it to inject large amounts of thermal energy
278 into the center of the galaxy.

279 The lower panel shows the virial mass of the subhalo, as
280 measured by M_{200} – the mass within the radius that encloses
281 a region of density $200\times$ the mean density of the universe.
282 Early on at $t < 4$ Gyr the virial mass grows roughly linearly up
283 to $\sim 2 \times 10^{12} M_{\odot}$. After that, the virial mass remains roughly
284 constant until sharp increases at $t \sim 10$ and ~ 12 Gyr. The
285 transition in the virial mass from linear to constant at $t \sim$
286 4 Gyr is followed 1 Gyr later by a sudden drop in the SFR
287 and BH accretion rate.

288 We show the evolution of the SoI in greater detail at the
289 transition between the high- and low- α sequences in Figure 4.

290 As in Figure 3, we indicate the SFR (blue) and black hole
291 accretion rate (orange), but we also include the strength of the
292 bar, taken to be the maximum value of A_2 in the bar region, in
293 red. From ~ 2.8 Gyr to ~ 3.2 Gyr, the SFR drops from ~ 54
294 to $3.6 M_{\odot}/\text{yr}$. The minimum in the SFR is nearly coincident
295 with the transition line.

296 We can see more clearly here that the BH accretion rate
297 (red), in units of the Eddington accretion rate, increases from
298 a value of ~ 0.08 at ~ 2.8 Gyr to a maximum of ~ 0.3 at
299 ~ 3.1 Gyr, right before the transition. This rise in the AGN
300 accretion rate is preceded by a strengthening of the bar, which
301 rises from an A_2 of ~ 0.1 at $t \sim 2.4$ Gyr to an A_2 of ~ 0.5 at
302 ~ 3.1 Gyr, the time of the peak BH accretion rate.

3.4. Images

303 In order to better conceptualize the evolution of the SoI at
304 the high- to low- α transition, we show surface density projec-
305 tions of the stellar (Figure 5) and gaseous (Figure 6) phases of
306 the progenitors of our SoI at various redshifts. In addition to
307 the final, $z = 0$, snapshot in the lower right, we show panels
308 for snapshots 23 to 36 in which z ranges from ~ 3.5 to ~ 1.7

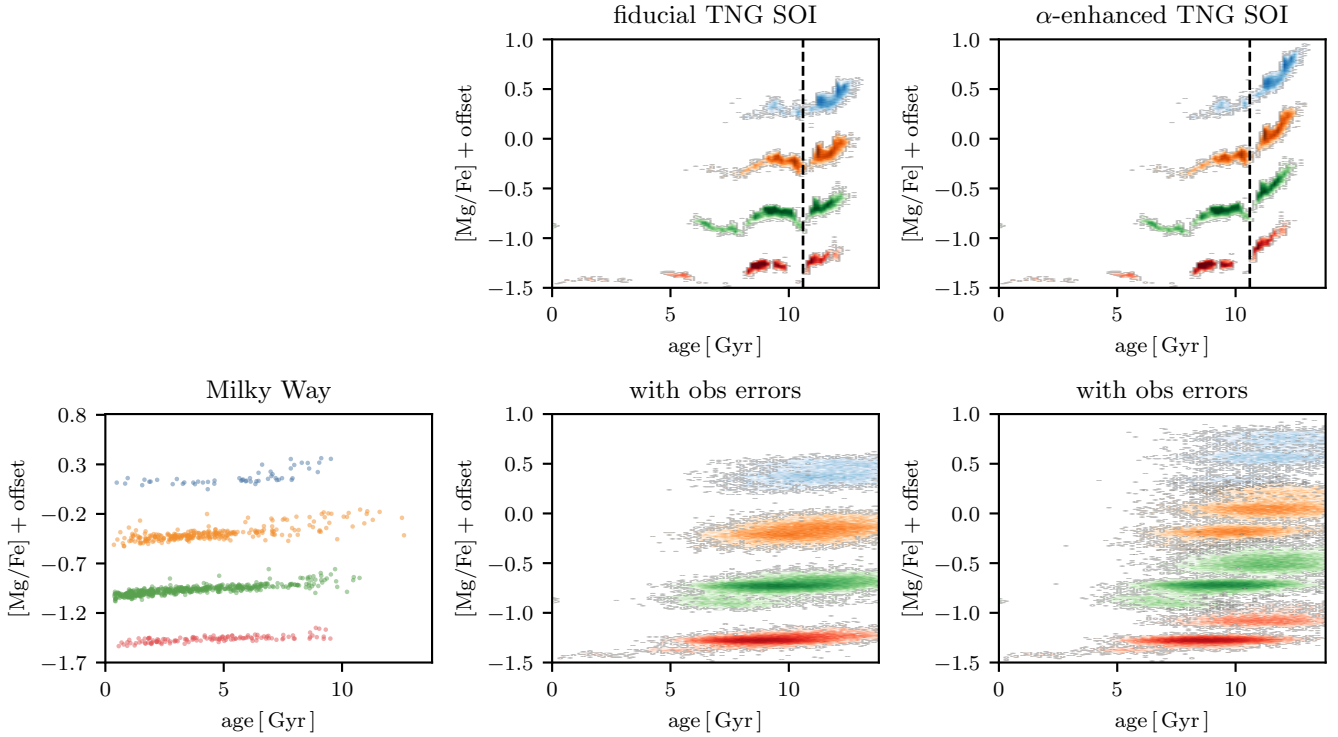


Figure 2. Bimodality in the abundance plane is linked to distinct epochs in simulation. The upper panels show $[\text{Mg}/\text{Fe}]$ as a function of age for our subhalo in TNG. The colors indicate stellar populations at fixed values of $[\text{Fe}/\text{H}]$, which are the same as in Figure 1. A gap in the relation occurs at an age of approximately 10.6 Gyr, which we indicate with a vertical dashed line. The effect of the α -enhancement is clear, as it separates the stars that form before and after this gap in ages (star particles which formed before $z = 1.5$ are α -enhanced, which occurs at an age of ~ 9.5 Gyr). The lower panels show on the left the Milky Way and on the center and right the data from TNG but with 15% age errors and 0.01 dex errors in $[\text{Mg}/\text{Fe}]$. When the simulations are given these errors, we see that the before and after star particles smear such that the two populations significantly overlap in ages. In the α -enhanced SoI, two populations emerge in each bin which overlapped in the fiducial distribution. This feature more closely resembles the Milky Way, which displays such populations where the bimodality is strongest – $[\text{Fe}/\text{H}] = -0.5$ (blue) and -0.25 (orange).

and the cosmic time from ~ 1.81 to ~ 3.74 Gyr. Projections are made on a 256×256 grid of a 25 kpc by 25 kpc square. All star particles/gas cells within ten times the stellar half-mass radius are used, and a simple nearest neighbor assignment of mass to each cell is used. Colors range logarithmically from 5×10^{-4} to 0.5 in native units ($10^{10} h M_{\odot} \text{ ckpc}^{-2}$), and only resolution elements within 10 times the stellar half-mass radius of the center of the subhalo are used.

We also show four relevant statistics in each panel of Figures 5 and 6. For Figure 5, these are, clockwise from the upper left, the SFR, cosmic time, bar strength, and BH accretion rate. They are the same for Figure 6, but bar strength is replaced with gas fraction (within twice the stellar half-mass radius). The bar strength is missing from several snapshots because the Zana et al. (2022) catalog excludes certain galaxies from being considered barred if they do not pass certain quality cuts. These can come from, e.g., flybys or violent buckling events.

A description of the events portrayed in each Figure is given in Section 4.4.

3.5. One-Zone Model

We showed in Figure 1 that a time-linear α -enhancement of old stars (forming before $z = 1.5$) led to the emergence of a strong chemical bimodality. This α -enhancement is equivalent to saying that $[\alpha/\text{Fe}]$ declines more rapidly with time at high- z . In Figure 7 we demonstrate an argument for why this steeper decline in $[\alpha/\text{Fe}]$ might be absent in TNG.

We show in the upper panel the evolution of $[\text{Mg}/\text{Fe}]$ of three one zone chemical evolution models which vary the star formation (SF) timescale. This timescale, τ_{\star} , is the inverse of the SF efficiency. A shorter SF timescale leads to a more rapid reduction in $[\text{Mg}/\text{Fe}]$. In the shortest timescale model, $\tau_{\star} = 0.5$ Gyr, $[\text{Mg}/\text{Fe}]$ drops from ~ 0.45 to 0.08 dex in 2 Gyr. In comparison, the longest timescale model, $\tau_{\star} = 5$ Gyr only drops to ~ 0.2 dex in the same time.

The lower panel shows the negative of the time derivative of $[\text{Mg}/\text{Fe}]$. This panel shows the same behavior, with the slope of the $\tau_{\star} = 0.5$ Gyr model peaking at -0.5 dex/Gyr compared to the 5 Gyr model which peaks at -0.25 dex/Gyr. After 1 Gyr, the trend starts to reverse, with the longer SF

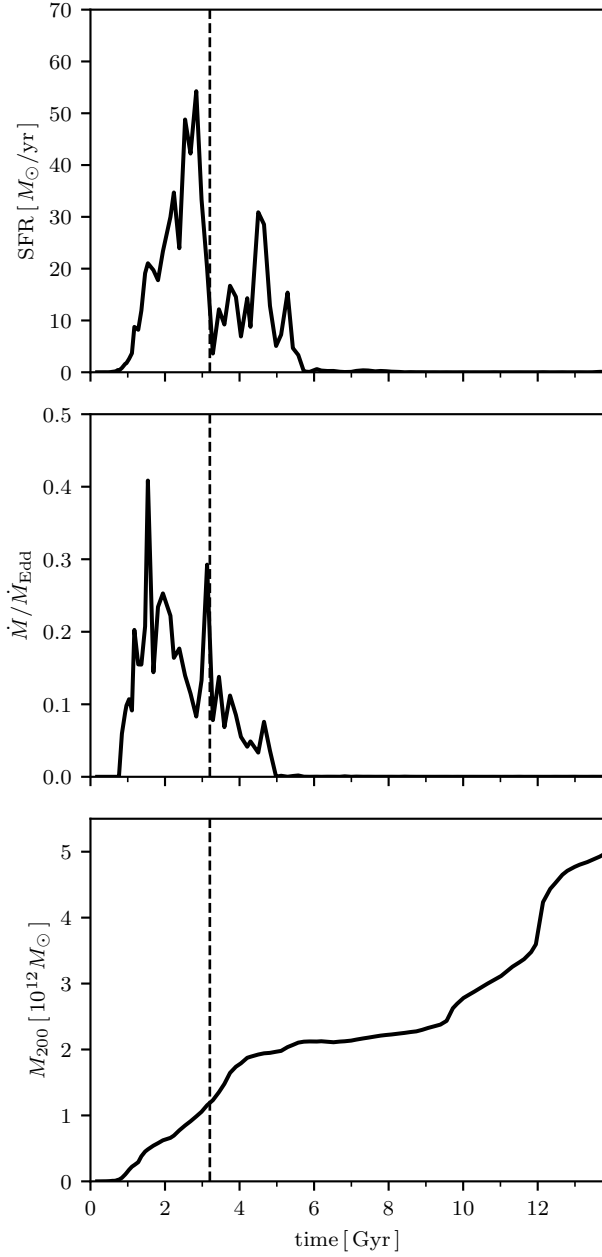


Figure 3. The evolutionary history of our subhalo of interest. The upper panel shows the SFH of our subhalo. This SFH is computed using the SFR within twice the stellar half-mass radius in our SoI's main progenitors. In this and all subsequent panels we show a vertical dashed line at the same position as in Figure 2 (~ 3.2 Gyr), which delineates the separation between the high- and low- α sequences. The gap in ages is naturally associated with a gap in the SFH located at the dashed line. The middle panel shows the BH accretion rate as a fraction of the maximum (Eddington) accretion rate across time. The accretion rate is high early on, but then drops. The gap in ages (dashed line) is coincident with a local peak in the BH accretion rate. In the lower panel we show the mass assembly of the halo, given as the mass within the radius that encloses 200× the mean density of the universe. In this plot mergers are shown as sudden increases in M_{200} . Mergers at very early times when the halo is significantly less massive than its $z = 0$ mass are not shown, but one can see that no clear merger is associated with the gap in stellar ages. Two mergers occur later on at $t \sim 10$ and ~ 12 Gyr.

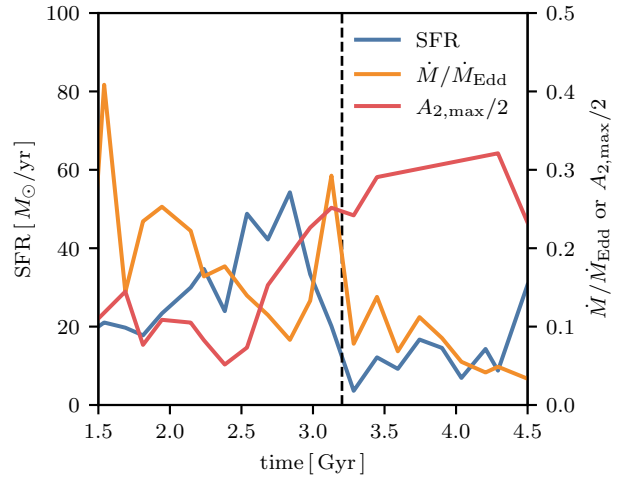


Figure 4. At the transition from the high- to low- α sequence, a bar forms and strengthens, AGN activity is enhanced, and star formation is suppressed. The evolutionary history of our SoI near the transition between the high- and low- α sequence, which is indicated as a vertical dashed line at an age of 10.6 Gyr ($t \sim 3.2$ Gyr). The blue line indicates the SFR, which drops from a peak of $\sim 54 M_{\odot}/\text{yr}$ to $\sim 3.6 M_{\odot}/\text{yr}$. The minimum is very close to the transition. The drop in SFR is coincident with a rise in the AGN accretion rate (orange) as well as a rise in the strength of the bar (red).

timescale models declining more rapidly, though at a much reduced rate (~ -0.1 dex/Gyr) than at the peak.

4. DISCUSSION

In Figure 1, we compared the abundance plane between the Milky Way and our SoI before and after the α -enhancement. It is visibly obvious that the TNG SoI is unimodal before the α -enhancement and bimodal afterwards (ignoring the minor mode at high-[Mg/Fe]). Here, we briefly discuss two main points: (1) assuming the α -enhancement is justified, what leads to the bimodality in the SoI?, and (2) what justifies the α -enhancement? We then briefly extend our comparison to the Milky Way data.

4.1. Cause of Bimodality

An extensive analysis of our SoI is beyond the scope of this project, but here we argue that the evidence is consistent with the scenario presented in Beane (2024). They presented an idealized simulation resembling the merger between the Milky Way and GSE. They varied the orbital parameters slightly in a grid of 27 simulations and found that simulations which had a brief quiescent period as a result of the merger led to a bimodal abundance distribution. They argued that AGN activity was responsible for this brief quenching.

Once the α -enhancement post-processing has been done, the SoI that we have studied in this work is consistent with

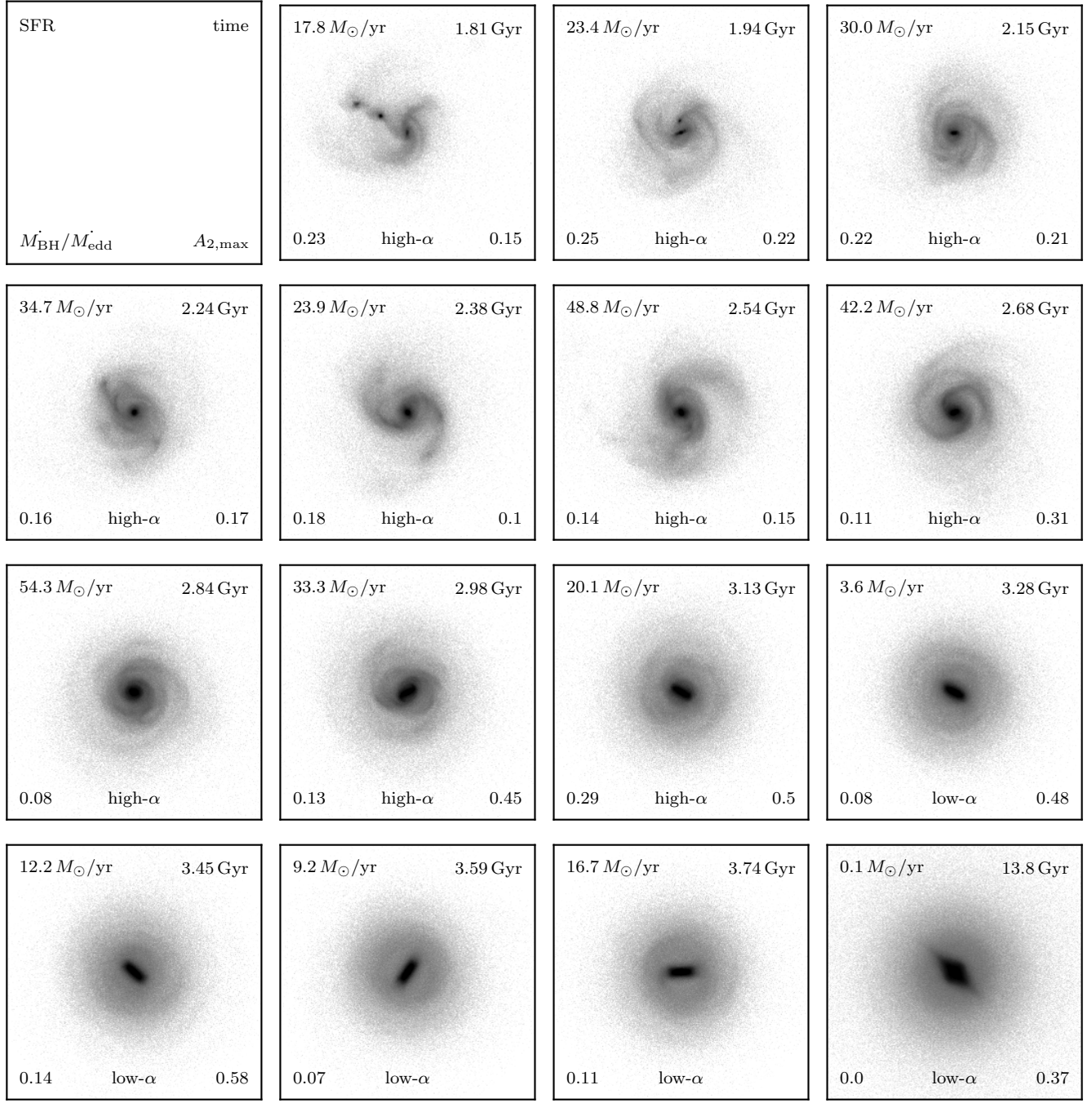


Figure 5. Surface density projections of star particles in our SoI at the transition between the high- and low- α sequences. Each panel indicates subsequent snapshots ranging from snapshot 23 ($z \sim 3.5$) to snapshot 36 ($z \sim 1.7$), as well as snapshot 99 ($z = 0$) in the lower right. Several key numbers are shown in the corners of each panel, clockwise from the top left: SFR, time, bar strength ($A_{2,\text{max}}$), and BH accretion rate. A guide is given in the top left subpanel. At the center-bottom of each panel, we indicate panels which occur before the transition (~ 3.2 Gyr) as high- α and panels which occur after as low- α .

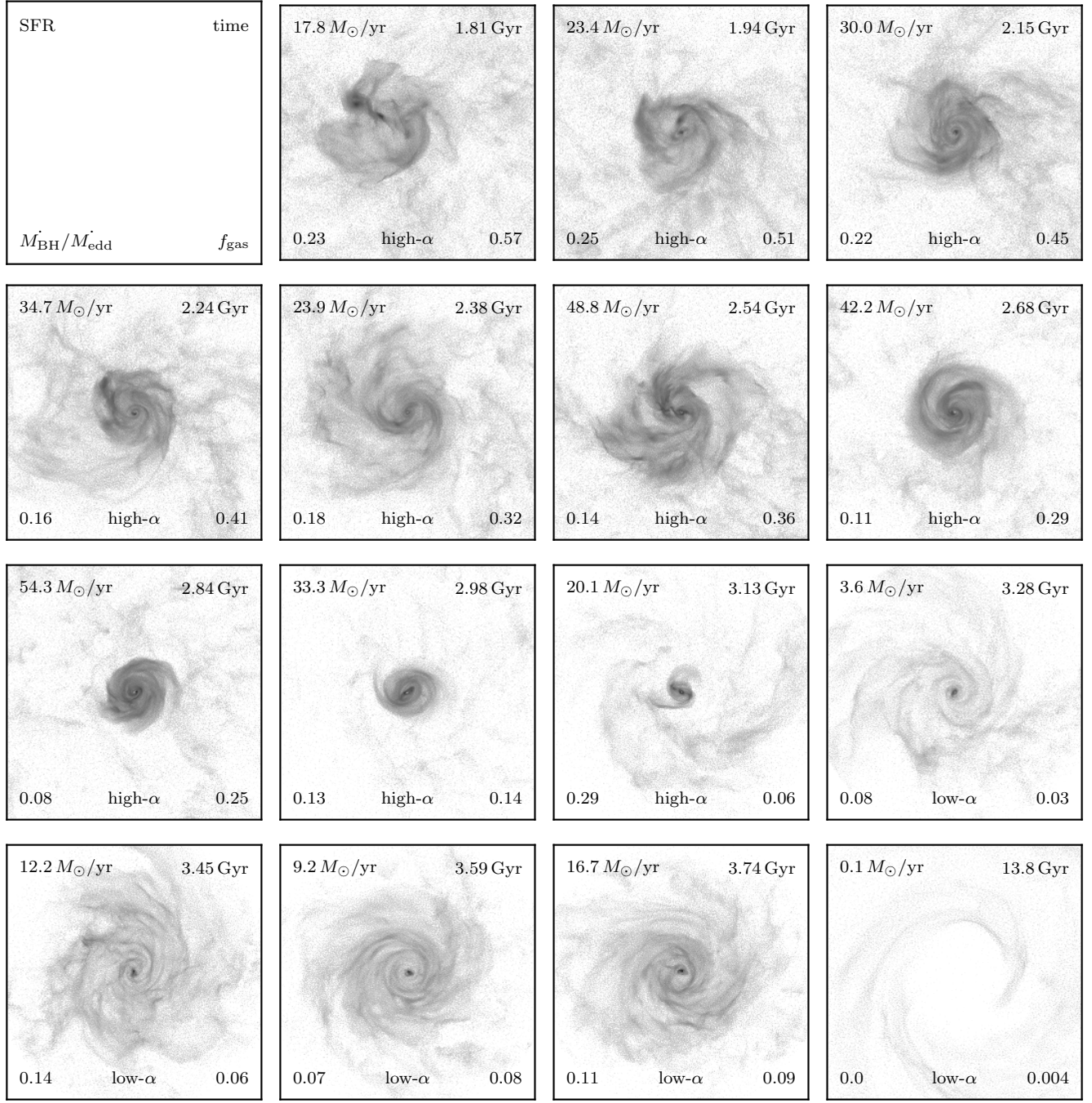


Figure 6. As in Figure 5, but showing the surface density projections of gas in our SoI at the transition between the high- and low- α sequences. Each panel indicates subsequent snapshots ranging from snapshot 23 ($z \sim 3.5$) to snapshot 36 ($z \sim 1.7$), as well as snapshot 99 ($z = 0$) in the lower right. Several key numbers are shown in the corners of each panel, clockwise from the top left: SFR, time, gas fraction, and BH accretion rate. A guide is given in the top left subpanel. At the center-bottom of each panel, we indicate panels which occur before the transition ($\sim 3.2 \text{ Gyr}$) as high- α and panels which occur after as low- α .

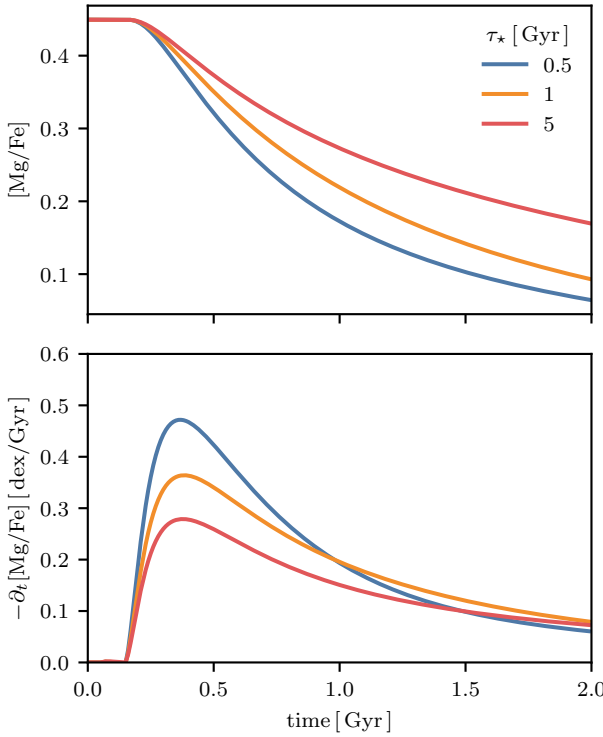


Figure 7. A higher star formation efficiency leads to a steeper decline in [Mg/Fe]. In both panels, the lines show the time evolution of [Mg/Fe] in a simple one zone chemical evolution model, described in Section 2.4. The upper panel shows the evolution of [Mg/Fe] over 2 Gyr while the lower panel shows the negative of its time derivative. Decreasing the star formation timescale $\tau_\star = M_{\text{gas}}/\text{SFR}$ leads to a more rapid decline in [Mg/Fe]. At its steepest decline ($t \sim 0.5$ Gyr), an order of magnitude decrease in τ_\star leads to a slope nearly a factor of 2 larger. At later times ($t > 1$ Gyr), the models with smaller τ_\star reach their steady-state [Mg/Fe] value more quickly.

this scenario. The vertical dashed line in Figures 2 and 3 denotes the transition between the high- and low- α sequences. We place it at an age of 10.6 Gyr or a formation time of ~ 3.2 Gyr. The upper right panel of Figure 2 shows 2D histograms of [Mg/Fe] vs star particle age in fixed bins of [Fe/H] (each color is a different [Fe/H] bin, and an offset is given to [Mg/Fe] so their medians are at zero). Stars which formed before the dashed line had a steep decline of [Mg/Fe] with time, while the relation in star particles formed after the dashed line is much more flat. At the line, we see a gap in the [Fe/H] = -0.5 and -0.25 bins.

The age gap in each [Fe/H] bin of Figure 2 is contemporaneous with a minimum in the global SFR. We can see in the upper panel of Figure 3 that this dashed line lies almost exactly at the point of a local minimum in the SFH. This minimum, which is $\sim 3 M_\odot/\text{yr}$, is 10–15× smaller than the maximum before and after it.

During this period of suppressed SF, we argue that the relative lack of enrichment of Type II SNe which leads to a lower rate of Mg production. This leads to a rapid reduction in [Mg/Fe]. This, combined with a lack of SF in the first place, leads to a scarcity of star particles in the region intermediate between the high- and low- α sequences. A more in-depth explanation is given in Section 4.1 in Beane (2024).

In the fiducial TNG distribution shown in the upper middle panel of Figure 2, the same general behavior with respect to the dashed line is present. However, because the [Mg/Fe] decline before the dashed line is not as strong, star particles which formed before and after the dashed line overlap in the [Mg/Fe] distribution shown in Figure 1.

It is also worth noting that in both the fiducial and α -enhanced SoI, there is a sort of rebound effect in [Mg/Fe]. The star particles which form directly after the dashed line have a slightly lower [Mg/Fe] than stars which form after. This was seen in Figure 9 of Beane (2024). In that work, it was argued that this occurs because, during the period of suppressed SF, the $[\alpha/\text{Fe}]$ of star forming gas plummets since there is no contribution from Type II SNe. Later, the $[\alpha/\text{Fe}]$ of the gas will recover when the SFR also recovers, but there is a brief window when old, low- α stars can form.

4.2. Steepening of α Decline

As described in Section 2.1, we applied a post-processing to the [Mg/Fe] of star particles in the TNG simulation. Specifically, for star particles formed before $z = 1.5$, we added to their [Mg/Fe] a value of $0.1 \times (t_{1.5} - t_{\text{form}})$, where $t_{1.5}$ is the age of the universe at $z = 1.5$ (~ 4.3 Gyr) and t_{form} is the formation time. This post-processed subhalo is presented alongside the fiducial subhalo in the right and middle columns, respectively, of Figures 1 and 2.

The [Mg/Fe] value of star forming gas is the result of a complicated mixture of many different aspects of the TNG model, to name a few: stellar and AGN feedback which alter gas inflows and outflows, secular, dynamical evolution, SF prescription, magnetic fields, (lack of) cosmic rays, diffusivity of hydrodynamics solver, and, of course, enrichment models. Isolating the cause of the “incorrect”¹ [Mg/Fe] vs time evolution at high- z is not straightforward nor, in our opinion, even possible. However, we do offer one reasonable explanation – the SFE at high densities, more present at high- z , is too low.

We demonstrate the impact of the SFE on the $[\alpha/\text{Fe}]$ ratio using a simple one-zone chemical evolution model with the publicly available code VICE. The details of our setup is given in Section 2.4. We vary the SF timescale, $\tau_\star = M_{\text{gas}}/\text{SFR}$,

¹Our case study of a single galaxy, selected in a non-reproducible manner, is hardly cause to firmly assert that the fiducial evolution in TNG50 is incorrect.

and examine the impact on the [Mg/Fe] ratio as a function of time. We find that shorter SF timescales do lead to a more rapid reduction in [Mg/Fe]. The rate of decrease in [Mg/Fe], at its maximum, varies from ~ -0.25 dex/Gyr in the $\tau_\star = 5$ Gyr model to ~ -0.5 dex/Gyr in the $\tau_\star = 0.5$ Gyr model. For our post-processing, assumed an additional decrease rate of 0.1 dex/Gyr. Such a difference is well within the range of [Mg/Fe] decrease seen in our different τ_\star models.

S. Hassan et al. (in preparation) demonstrated that the pressure regulated feedback model of Ostriker & Kim (2022) predicts higher SFRs of patches of gaseous disks in TNG50 than the fiducial model by up to an order of magnitude. This is well within our needed factor of 2 in τ_\star . Therefore, our argument that the [Mg/Fe] does not decline quickly enough at high- z is reasonably justified. An intuitive understanding of the impact the decline in $[\alpha/\text{Fe}]$ vs time has is that, when $[\alpha/\text{Fe}]$ declines rapidly, it is a better estimator of age. When it is a better estimator of age, events which are separated temporally become better separated in the abundance plane.

4.3. Comparison to Observations

The lower left panel of Figure 2 shows the [Mg/Fe] vs age of stars in bins of [Fe/H] which pass our solar neighborhood selection and are present in the APOKASC2 catalog. In the bins where the bimodality is strongest (blue and orange, $[\text{Fe}/\text{H}] = -0.5$ and -0.25 , respectively), we see that there is a sort of two tiered distribution with significant overlap in age. In the SoI with age and abundance errors shown in the lower right panel, a very similar distribution can be seen in all [Fe/H] bins. An examination of the true distribution in the SoI (upper right panel), we see that the two distributions are in fact very cleanly separated in age. We do not know the true underlying distribution in the Milky Way, but these panels show that the general picture shown in our SoI is consistent with the Milky Way.

4.4. Cause of Quiescence

It is natural to question why the minimum in the SFR occurs. In Beane (2024), AGN activity from a merger was the suspected cause. Here, we can see that there is indeed a brief burst in AGN accretion at the time of the merger (middle panel of Figure 3). Based on this burst, it is reasonable to suspect that AGN activity is also responsible for the quiescent period in our SoI. However, we argue that the cause of the localized spike in the BH accretion rate is not due to a merger but instead due to the formation/strengthening of a bar.

In Figure 4, we take a closer view of the evolution of our SoI at the transition between the high- and low- α sequence, which we denote with the same line at an age of 10.6 Gyr ($t \sim 3.2$ Gyr) as before. Here, we see that indeed the drop in the SFR ($\sim 3.6 M_\odot/\text{yr}$ at $t \sim 3.3$ Gyr) reaches a minimum one snapshot after the maximum in the BH accretion rate ($\sim 0.3 \times \dot{M}_{\text{edd}}$ at $t \sim 3.1$ Gyr).

The gaseous surface density images in Figure 6 are helpful to understand this moment in the SoI's history. The third row, from $t = 2.84$ to 3.28 Gyr shows this moment, with the rightmost $t = 3.28$ Gyr marking the transition from high- to low- α formation. The gas fraction (bottom right number) quickly drops from 25% to 3%, accompanied by not only a high SFR ($54.3 M_\odot/\text{yr}$ at maximum) but also an increasing BH accretion rate.

This increasing BH accretion rate is also preceded by the formation of a stellar bar at the center of the galaxy as seen in Figure 5.² Starting from $t = 2.38$ Gyr, the bar strength grows from $A_{2,\text{max}} = 0.1$ to 0.5 at $t = 3.13$ Gyr, the peak of the BH accretion rate. Note that the bar strength considers only the region where the phase of the second Fourier mode is constant, and so spiral structure as seen in, e.g., the $t = 2.38$ Gyr snapshot is not eligible for $A_{2,\text{max}}$.

The scenario implied by all the available evidence is that:

1. a bar forms through an internal instability, which
2. drives a large amount of gas to the center of the galaxy, which
3. triggers a high BH accretion rate and quasar-mode thermal feedback, which
4. clears gas out of the galaxy.

This picture is supported by work showing that in simulations bars should be able to fuel AGN (Shlosman et al. 1990; Hopkins & Quataert 2010), and that barred galaxies preferentially host AGN (Silva-Lima et al. 2022). At high- z , the AGN mechanism is thought to be responsible for quenching (e.g. D'Eugenio et al. 2023; Park et al. 2024; Mićić et al. 2024; Belli et al. 2024, and references therein).

A complicating factor for this picture comes from the high SFR associated with the galaxy. The depletion time ($M_{\text{gas}}/\text{SFR}$) at the $t = 2.84$ Gyr snapshot is 204 Myr, shorter than the time it takes for the SFR to reach its minimum. However, this has to be balanced by the fact that the depletion time is already short at this redshift. The average depletion time in the preceding 5 snapshots is 220 Myr, so clearly the SoI is accreting high amounts of gas from its CGM. A definitive account, difficult with the current simulation because of its sparse snapshot spacing, requires further work.

5. CONCLUSIONS

In this work, we examined a specific subhalo in Illustris TNG50. This subhalo is at a Milky Way-progenitor mass at high- z ($z \sim 2$). After applying a post-processing step that increased the [Mg/Fe] of star particles formed before $z = 1.5$,

²The bar is already at a strength of $A_{2,\text{max}} \sim 0.1$ before, so it either forms or strengthens depending on one's interpretation. We choose the former.

535 this subhalo hosts a strong bimodality in the plane of [Mg/Fe]
 536 and [Fe/H], shown in Figure 1. This post-processing is jus-
 537 tified by arguing that the SFE of dense gas is too low in TNG
 538 (Section 4.2).

539 This bimodality can be traced to an event that occurred at
 540 an age of 10.6 Gyr, or formation time of ~ 3.2 Gyr ($z \sim 2$).
 541 Shown as a vertical dashed line in Figure 2, star particles
 542 which form before this form at high- α while stars which form
 543 after form at lower α . At the dashed line, there is a gap. We ar-
 544 gue that the presence of this gap is responsible for the valley
 545 in the bimodality (Figure 1). It is accompanied by a global
 546 reduction in the SFR by about a factor of 6 (upper panel of
 547 Figure 3).

548 The reduction in the SFR has two effects. First, a lower
 549 production of Mg is the natural result of a lack of Type II
 550 SNe. Second, the lack of SF means that stars at [Mg/Fe]
 551 intermediate between the high- and low- α sequences never
 552 form. This is the same argument that was first presented in
 553 Beane (2024). When observational errors are added to the

554 subhalo’s abundance vs age distribution, we show that it is
 555 broadly consistent with the Milky Way’s abundance-age dis-
 556 tribution (Section 4.3).

557 While a strong claim about the cause of the quiescent
 558 period is difficult to make, we showed that the forma-
 559 tion/strengthening of a bar could be responsible for triggering
 560 an episode of AGN activity. This work adds further support
 561 that the argument made in Beane (2024) is a plausible expla-
 562 nation for the Milky Way’s abundance bimodality.

563 This work has made use of data from the European Space
 564 Agency (ESA) mission *Gaia* (<https://www.cosmos.esa.int/gaia>), processed by the *Gaia* Data Processing and Anal-
 565 ysis Consortium (DPAC, <https://www.cosmos.esa.int/web/gaia/dpac/consortium>). Funding for the DPAC has been pro-
 566 vided by national institutions, in particular the institutions
 567 participating in the *Gaia* Multilateral Agreement.

REFERENCES

- 570 Adibekyan, V. Z., Santos, N. C., Sousa, S. G., & Israelian, G. 2011,
 571 A&A, 535, L11, doi: [10.1051/0004-6361/201118240](https://doi.org/10.1051/0004-6361/201118240)
- 572 Adibekyan, V. Z., Sousa, S. G., Santos, N. C., et al. 2012, A&A,
 573 545, A32, doi: [10.1051/0004-6361/201219401](https://doi.org/10.1051/0004-6361/201219401)
- 574 Beane, A. 2024, arXiv e-prints, arXiv:2407.07985,
 575 doi: [10.48550/arXiv.2407.07985](https://doi.org/10.48550/arXiv.2407.07985)
- 576 Belli, S., Park, M., Davies, R. L., et al. 2024, Nature, 630, 54,
 577 doi: [10.1038/s41586-024-07412-1](https://doi.org/10.1038/s41586-024-07412-1)
- 578 Belokurov, V., Erkal, D., Evans, N. W., Koposov, S. E., & Deason,
 579 A. J. 2018, MNRAS, 478, 611, doi: [10.1093/mnras/sty982](https://doi.org/10.1093/mnras/sty982)
- 580 Bensby, T., Feltzing, S., & Oey, M. S. 2014, A&A, 562, A71,
 581 doi: [10.1051/0004-6361/201322631](https://doi.org/10.1051/0004-6361/201322631)
- 582 Bernaldo e Silva, L., Debattista, V. P., Khachaturyants, T., &
 583 Nidever, D. 2020, MNRAS, 492, 4716,
 584 doi: [10.1093/mnras/staa065](https://doi.org/10.1093/mnras/staa065)
- 585 Bernaldo e Silva, L., Debattista, V. P., Nidever, D., Amarante, J.
 586 A. S., & Garver, B. 2021, MNRAS, 502, 260,
 587 doi: [10.1093/mnras/staa3966](https://doi.org/10.1093/mnras/staa3966)
- 588 Bland-Hawthorn, J., & Gerhard, O. 2016, ARA&A, 54, 529,
 589 doi: [10.1146/annurev-astro-081915-023441](https://doi.org/10.1146/annurev-astro-081915-023441)
- 590 Bondi, H. 1952, MNRAS, 112, 195, doi: [10.1093/mnras/112.2.195](https://doi.org/10.1093/mnras/112.2.195)
- 591 Bondi, H., & Hoyle, F. 1944, MNRAS, 104, 273,
 592 doi: [10.1093/mnras/104.5.273](https://doi.org/10.1093/mnras/104.5.273)
- 593 Brook, C., Richard, S., Kawata, D., Martel, H., & Gibson, B. K.
 594 2007, ApJ, 658, 60, doi: [10.1086/511056](https://doi.org/10.1086/511056)
- 595 Brook, C. B., Gibson, B. K., Martel, H., & Kawata, D. 2005, ApJ,
 596 630, 298, doi: [10.1086/431924](https://doi.org/10.1086/431924)
- 597 Brook, C. B., Kawata, D., Gibson, B. K., & Freeman, K. C. 2004,
 598 ApJ, 612, 894, doi: [10.1086/422709](https://doi.org/10.1086/422709)
- 599 Buck, T. 2020, MNRAS, 491, 5435, doi: [10.1093/mnras/stz3289](https://doi.org/10.1093/mnras/stz3289)
- 600 Chandra, V., Semenov, V. A., Rix, H.-W., et al. 2024, ApJ, 972,
 601 112, doi: [10.3847/1538-4357/ad5b60](https://doi.org/10.3847/1538-4357/ad5b60)
- 602 Chen, B., Hayden, M. R., Sharma, S., et al. 2023, MNRAS, 523,
 603 3791, doi: [10.1093/mnras/stad1568](https://doi.org/10.1093/mnras/stad1568)
- 604 Chiappini, C. 2009, in The Galaxy Disk in Cosmological Context,
 605 ed. J. Andersen, Nordströra, B. m., & J. Bland-Hawthorn, Vol.
 606 254, 191–196, doi: [10.1017/S1743921308027580](https://doi.org/10.1017/S1743921308027580)
- 607 Chiappini, C., Matteucci, F., & Gratton, R. 1997, ApJ, 477, 765,
 608 doi: [10.1086/303726](https://doi.org/10.1086/303726)
- 609 Ciucă, I., Kawata, D., Ting, Y.-S., et al. 2024, MNRAS, 528, L122,
 610 doi: [10.1093/mnrasl/slad033](https://doi.org/10.1093/mnrasl/slad033)
- 611 Clarke, A. J., Debattista, V. P., Nidever, D. L., et al. 2019, MNRAS,
 612 484, 3476, doi: [10.1093/mnras/stz104](https://doi.org/10.1093/mnras/stz104)
- 613 D’Eugenio, F., Perez-Gonzalez, P., Maiolino, R., et al. 2023, arXiv
 614 e-prints, arXiv:2308.06317, doi: [10.48550/arXiv.2308.06317](https://doi.org/10.48550/arXiv.2308.06317)
- 615 Fuhrmann, K. 1998, A&A, 338, 161
 616 —. 2004, Astronomische Nachrichten, 325, 3,
 617 doi: [10.1002/asna.200310173](https://doi.org/10.1002/asna.200310173)
- 618 García Pérez, A. E., Allende Prieto, C., Holtzman, J. A., et al.
 619 2016, AJ, 151, 144, doi: [10.3847/0004-6256/151/6/144](https://doi.org/10.3847/0004-6256/151/6/144)
- 620 Garver, B. R., Nidever, D. L., Debattista, V. P., Bernaldo e Silva, L.,
 621 & Khachaturyants, T. 2023, ApJ, 953, 128,
 622 doi: [10.3847/1538-4357/acdfc6](https://doi.org/10.3847/1538-4357/acdfc6)
- 623 Gratton, R., Carretta, E., Matteucci, F., & Sneden, C. 1996, in
 624 Astronomical Society of the Pacific Conference Series, Vol. 92,
 625 Formation of the Galactic Halo...Inside and Out, ed. H. L.
 626 Morrison & A. Sarajedini, 307

- ⁶²⁷ Grisoni, V., Spitoni, E., Matteucci, F., et al. 2017, MNRAS, 472,
⁶²⁸ 3637, doi: [10.1093/mnras/stx2201](https://doi.org/10.1093/mnras/stx2201)
- ⁶²⁹ Hayden, M. R., Bland-Hawthorn, J., Sharma, S., et al. 2020,
⁶³⁰ MNRAS, 493, 2952, doi: [10.1093/mnras/staa335](https://doi.org/10.1093/mnras/staa335)
- ⁶³¹ Helmi, A., Babusiaux, C., Koppelman, H. H., et al. 2018, Nature,
⁶³² 563, 85, doi: [10.1038/s41586-018-0625-x](https://doi.org/10.1038/s41586-018-0625-x)
- ⁶³³ Hopkins, P. F., & Quataert, E. 2010, MNRAS, 407, 1529,
⁶³⁴ doi: [10.1111/j.1365-2966.2010.17064.x](https://doi.org/10.1111/j.1365-2966.2010.17064.x)
- ⁶³⁵ Hoyle, F., & Lyttleton, R. A. 1939, Proceedings of the Cambridge
⁶³⁶ Philosophical Society, 35, 405,
⁶³⁷ doi: [10.1017/S0305004100021150](https://doi.org/10.1017/S0305004100021150)
- ⁶³⁸ Khoperskov, S., Haywood, M., Snaith, O., et al. 2021, MNRAS,
⁶³⁹ 501, 5176, doi: [10.1093/mnras/staa3996](https://doi.org/10.1093/mnras/staa3996)
- ⁶⁴⁰ Mićić, M., Irwin, J. A., Nair, P., et al. 2024, arXiv e-prints,
⁶⁴¹ arXiv:2405.18685. <https://arxiv.org/abs/2405.18685>
- ⁶⁴² Naidu, R. P., Conroy, C., Bonaca, A., et al. 2020, ApJ, 901, 48,
⁶⁴³ doi: [10.3847/1538-4357/abaef4](https://doi.org/10.3847/1538-4357/abaef4)
- ⁶⁴⁴ Nelson, D., Pillepich, A., Springel, V., et al. 2019, MNRAS, 490,
⁶⁴⁵ 3234, doi: [10.1093/mnras/stz2306](https://doi.org/10.1093/mnras/stz2306)
- ⁶⁴⁶ Nidever, D. L., Bovy, J., Bird, J. C., et al. 2014, ApJ, 796, 38,
⁶⁴⁷ doi: [10.1088/0004-637X/796/1/38](https://doi.org/10.1088/0004-637X/796/1/38)
- ⁶⁴⁸ Ostriker, E. C., & Kim, C.-G. 2022, ApJ, 936, 137,
⁶⁴⁹ doi: [10.3847/1538-4357/ac7de2](https://doi.org/10.3847/1538-4357/ac7de2)
- ⁶⁵⁰ Pakmor, R., Springel, V., Bauer, A., et al. 2016, MNRAS, 455,
⁶⁵¹ 1134, doi: [10.1093/mnras/stv2380](https://doi.org/10.1093/mnras/stv2380)
- ⁶⁵² Park, M., Belli, S., Conroy, C., et al. 2024, arXiv e-prints,
⁶⁵³ arXiv:2404.17945, doi: [10.48550/arXiv.2404.17945](https://doi.org/10.48550/arXiv.2404.17945)
- ⁶⁵⁴ Pillepich, A., Springel, V., Nelson, D., et al. 2018, MNRAS, 473,
⁶⁵⁵ 4077, doi: [10.1093/mnras/stx2656](https://doi.org/10.1093/mnras/stx2656)
- ⁶⁵⁶ Pillepich, A., Nelson, D., Springel, V., et al. 2019, MNRAS, 490,
⁶⁵⁷ 3196, doi: [10.1093/mnras/stz2338](https://doi.org/10.1093/mnras/stz2338)
- ⁶⁵⁸ Pinsonneault, M. H., Elsworth, Y. P., Tayar, J., et al. 2018, ApJS,
⁶⁵⁹ 239, 32, doi: [10.3847/1538-4365/aaebfd](https://doi.org/10.3847/1538-4365/aaebfd)
- ⁶⁶⁰ Reddy, B. E., Lambert, D. L., & Allende Prieto, C. 2006, MNRAS,
⁶⁶¹ 367, 1329, doi: [10.1111/j.1365-2966.2006.10148.x](https://doi.org/10.1111/j.1365-2966.2006.10148.x)
- ⁶⁶² Richard, S., Brook, C. B., Martel, H., et al. 2010, MNRAS, 402,
⁶⁶³ 1489, doi: [10.1111/j.1365-2966.2009.16008.x](https://doi.org/10.1111/j.1365-2966.2009.16008.x)
- ⁶⁶⁴ Schönrich, R., & Binney, J. 2009, MNRAS, 396, 203,
⁶⁶⁵ doi: [10.1111/j.1365-2966.2009.14750.x](https://doi.org/10.1111/j.1365-2966.2009.14750.x)
- ⁶⁶⁶ Sharma, S., Hayden, M. R., & Bland-Hawthorn, J. 2021, MNRAS,
⁶⁶⁷ 507, 5882, doi: [10.1093/mnras/stab2015](https://doi.org/10.1093/mnras/stab2015)
- ⁶⁶⁸ Shlosman, I., Begelman, M. C., & Frank, J. 1990, Nature, 345, 679,
⁶⁶⁹ doi: [10.1038/345679a0](https://doi.org/10.1038/345679a0)
- ⁶⁷⁰ Silva-Lima, L. A., Martins, L. P., Coelho, P. R. T., & Gadotti, D. A.
⁶⁷¹ 2022, A&A, 661, A105, doi: [10.1051/0004-6361/202142432](https://doi.org/10.1051/0004-6361/202142432)
- ⁶⁷² Spitoni, E., Matteucci, F., Gratton, R., et al. 2024, arXiv e-prints,
⁶⁷³ arXiv:2405.11025, doi: [10.48550/arXiv.2405.11025](https://doi.org/10.48550/arXiv.2405.11025)
- ⁶⁷⁴ Spitoni, E., Silva Aguirre, V., Matteucci, F., Calura, F., & Grisoni,
⁶⁷⁵ V. 2019, A&A, 623, A60, doi: [10.1051/0004-6361/201834188](https://doi.org/10.1051/0004-6361/201834188)
- ⁶⁷⁶ Springel, V. 2010, MNRAS, 401, 791,
⁶⁷⁷ doi: [10.1111/j.1365-2966.2009.15715.x](https://doi.org/10.1111/j.1365-2966.2009.15715.x)
- ⁶⁷⁸ van Dokkum, P. G., Leja, J., Nelson, E. J., et al. 2013, ApJL, 771,
⁶⁷⁹ L35, doi: [10.1088/2041-8205/771/2/L35](https://doi.org/10.1088/2041-8205/771/2/L35)
- ⁶⁸⁰ Vogelsberger, M., Genel, S., Sijacki, D., et al. 2013, MNRAS, 436,
⁶⁸¹ 3031, doi: [10.1093/mnras/stt1789](https://doi.org/10.1093/mnras/stt1789)
- ⁶⁸² Weinberger, R., Springel, V., Hernquist, L., et al. 2017, MNRAS,
⁶⁸³ 465, 3291, doi: [10.1093/mnras/stw2944](https://doi.org/10.1093/mnras/stw2944)
- ⁶⁸⁴ Zana, T., Lupi, A., Bonetti, M., et al. 2022, MNRAS, 515, 1524,
⁶⁸⁵ doi: [10.1093/mnras/stac1708](https://doi.org/10.1093/mnras/stac1708)

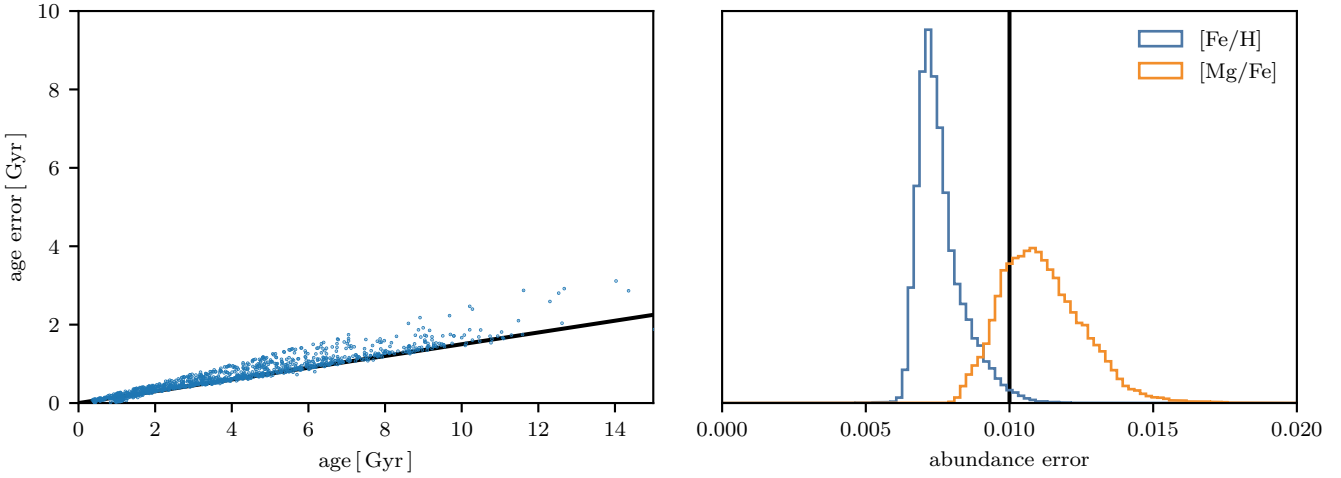


Figure 8. The observational errors of the APOKASC2 (left) and ASPCAP dataset (right). We show, on the left, a line indicating a 15% error in observed age and on the right a vertical line indicating a 0.01 dex error.

686

APPENDIX

687

A. OBSERVATIONAL ERRORS

688 In Figure 2, we assumed observational errors of 15% in age and 0.01 dex in [Mg/Fe]. In Figure 8, we plot the quoted ob-
 689 servational errors of the APOKASC2 (left) and ASPCAP (right) datasets, showing both [Fe/H] and [Mg/Fe] (blue and orange,
 690 respectively). We show our 15% age error and 0.01 dex abundance error assumptions as black lines. For the age error, we used
 691 the maximum of the upper and lower estimates from Pinsonneault et al. (2018). Our assumed errors are generally consistent with
 692 the errors. Our error in [Mg/Fe] is a bit smaller than in ASPCAP, but the age estimates are by far the more constraining of the
 693 two.

694

B. RANDOM SELECTION OF SUBHALOS

695 In Figures 9 to 25, we show a version of Figure 1 but for a random selection of subhalos from our broader sample of 168 Milky
 696 Way-progenitors at $z = 1.5$ in TNG50. It is from this sample that we selected our SoI. We first show our SoI at $z = 1.5$ in Figure 9,
 697 and then show our random sample of 16.

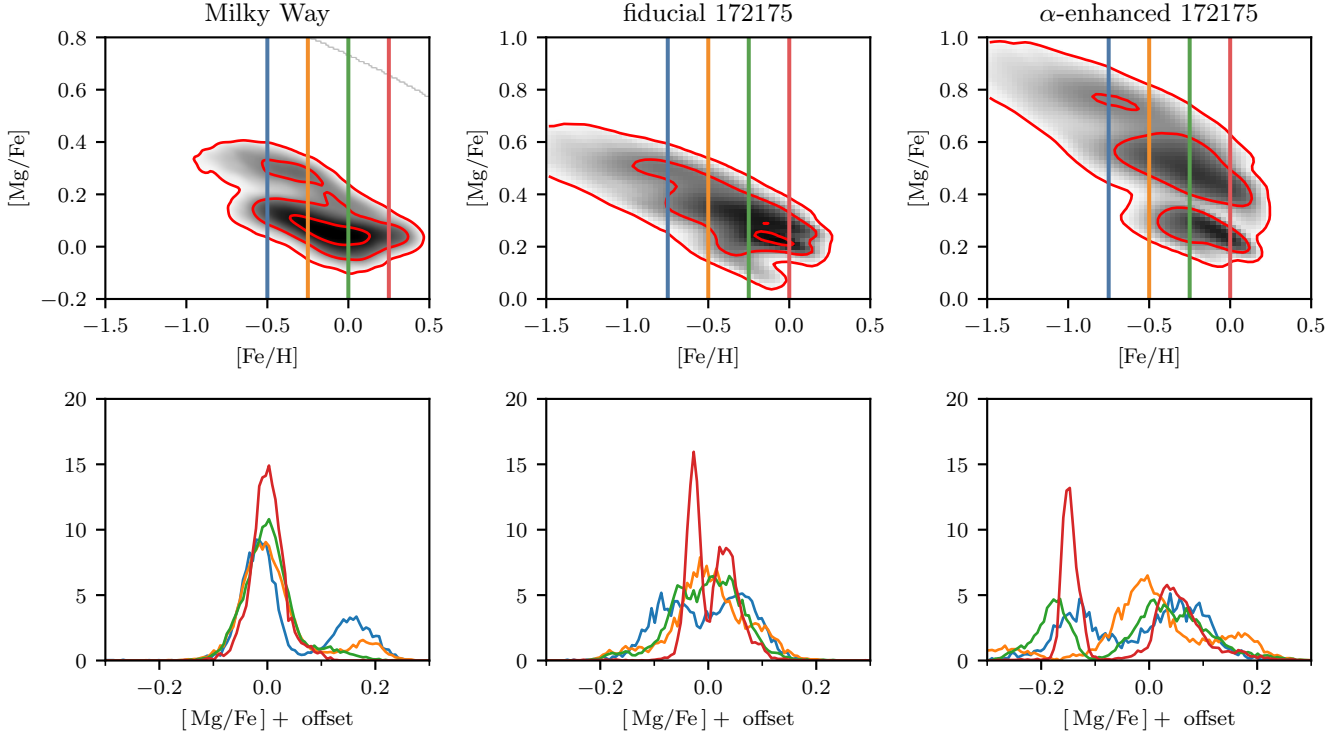


Figure 9. The same as Figure 1, but for our SoI at $z = 1.5$.

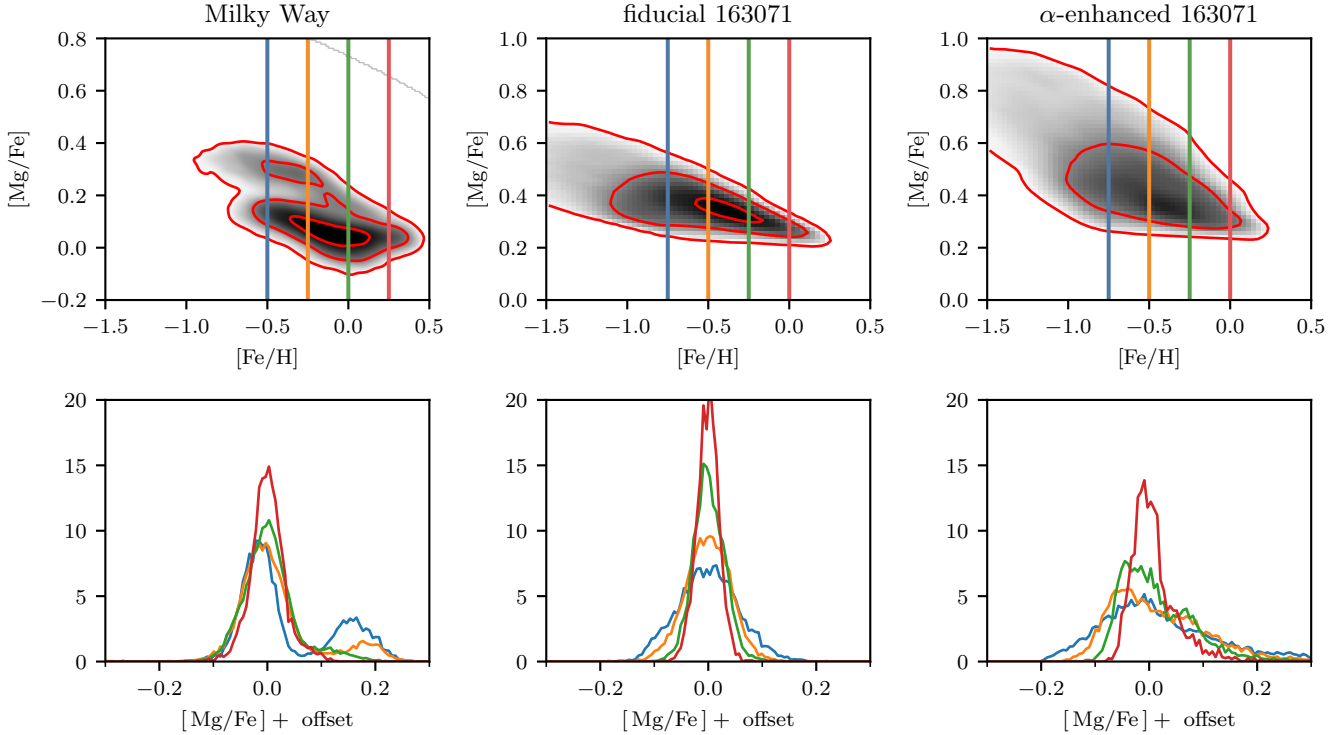


Figure 10. The same as Figure 1, but for a random subhalo from our catalog at $z = 1.5$.

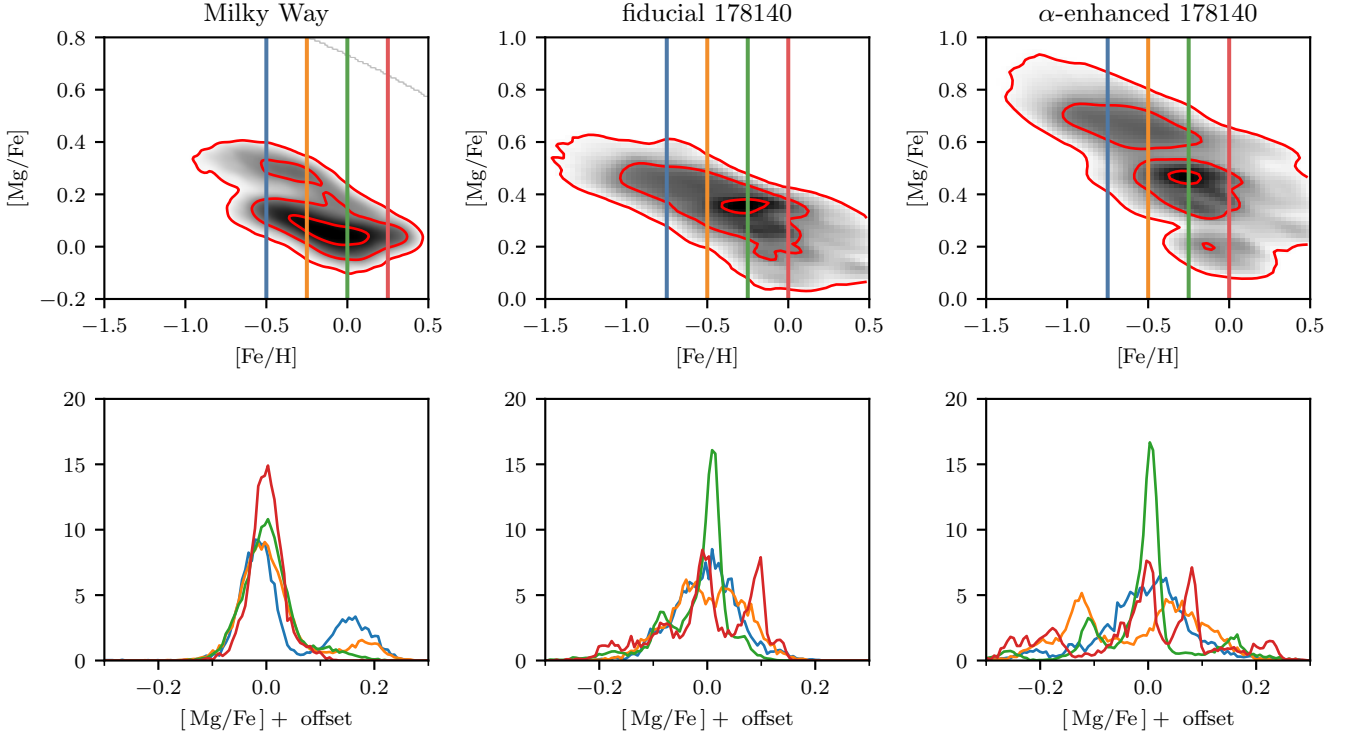


Figure 11. The same as Figure 1, but for a random subhalo from our catalog at $z = 1.5$.

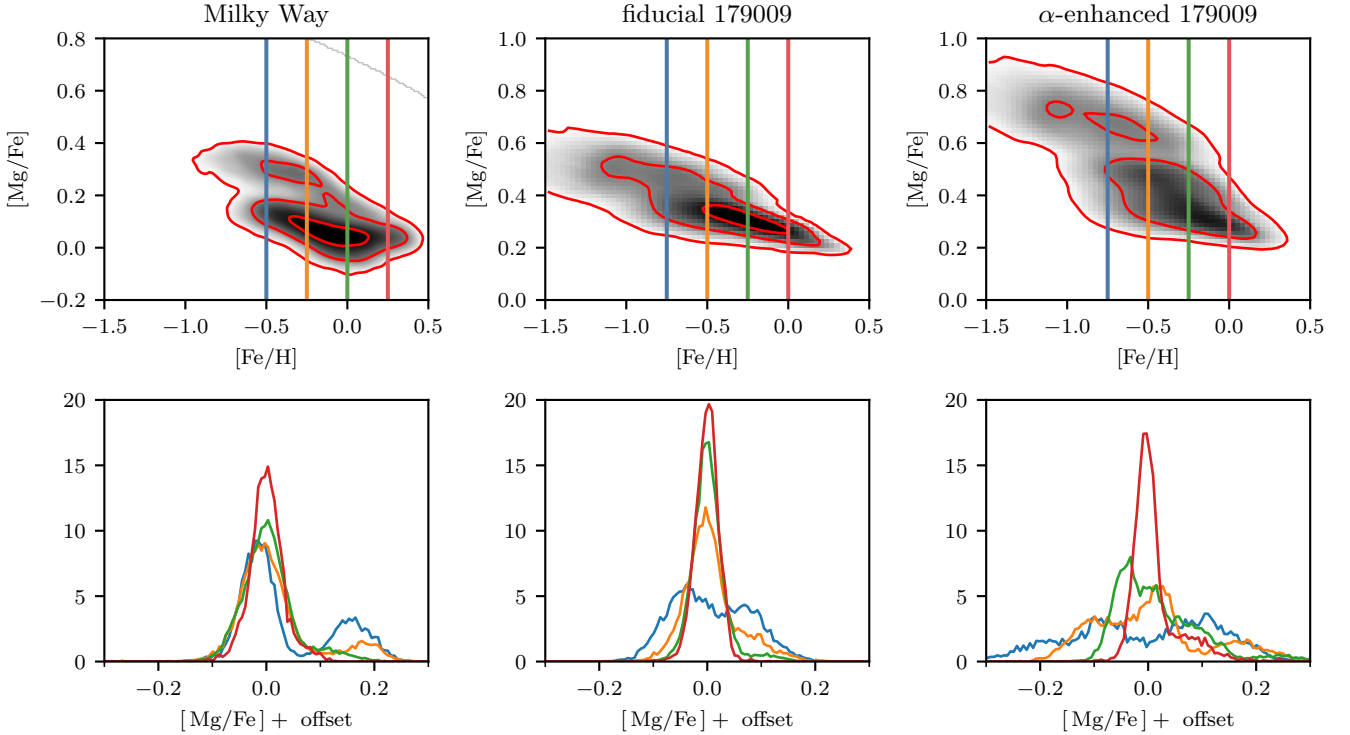


Figure 12. The same as Figure 1, but for a random subhalo from our catalog at $z = 1.5$.

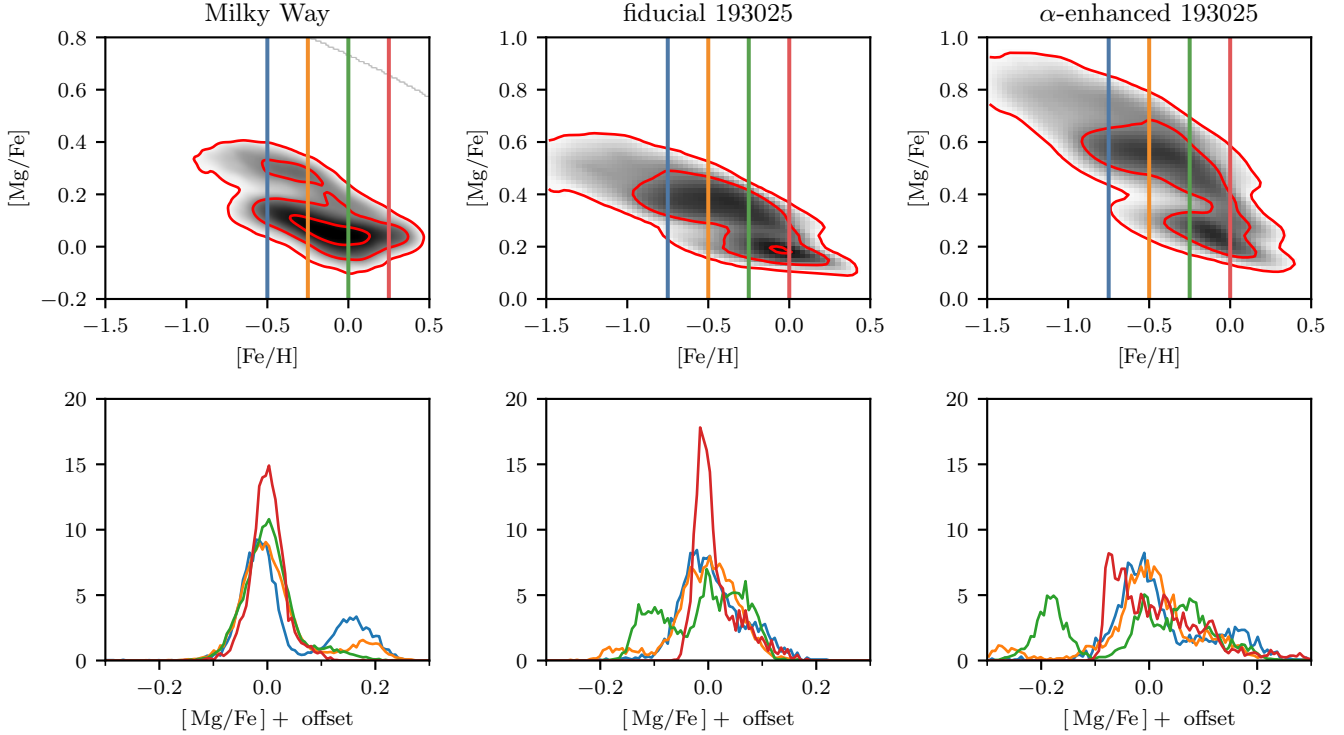


Figure 13. The same as Figure 1, but for a random subhalo from our catalog at $z = 1.5$.

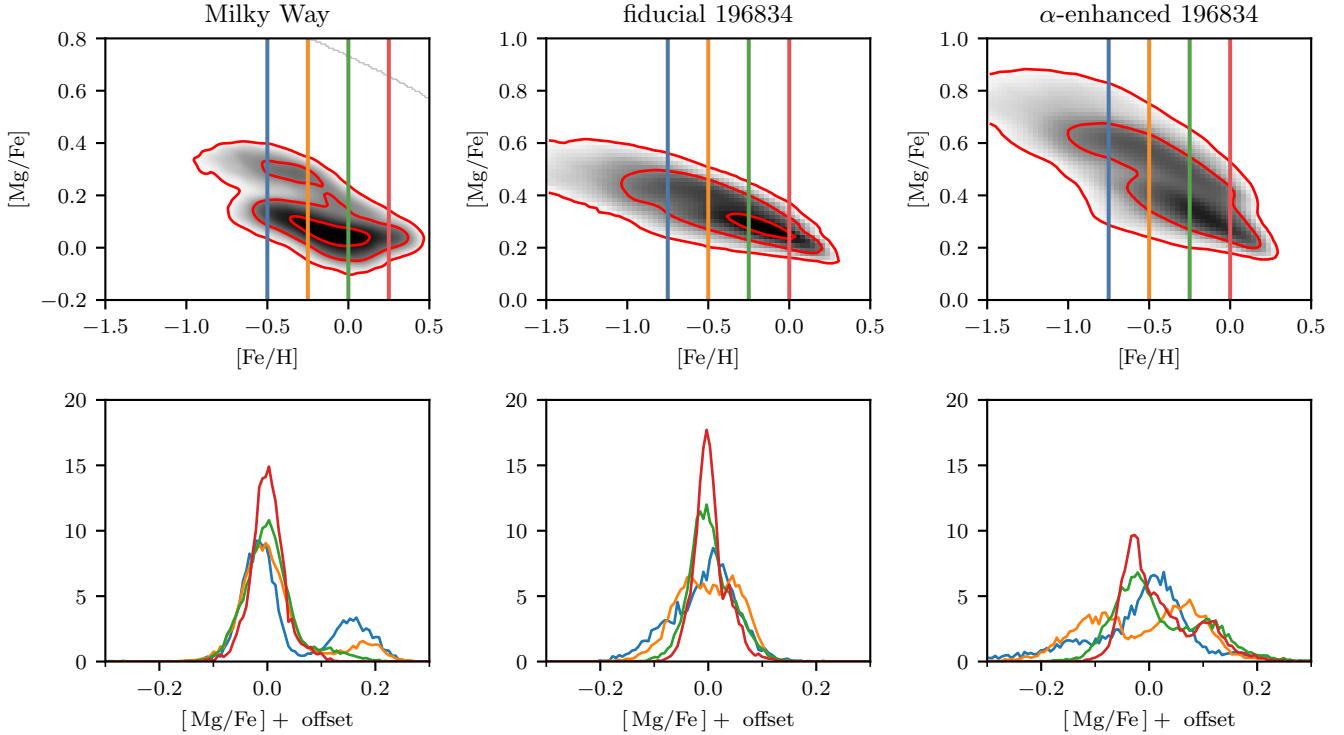


Figure 14. The same as Figure 1, but for a random subhalo from our catalog at $z = 1.5$.

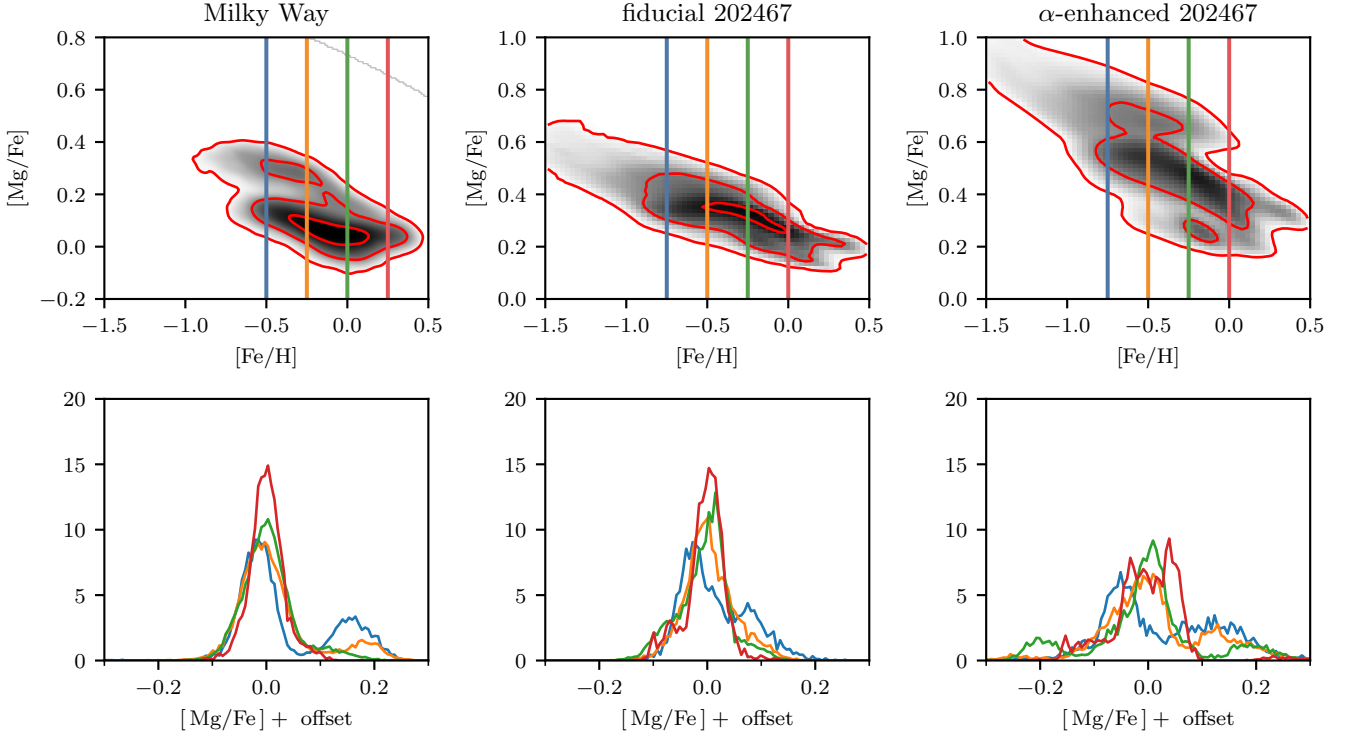


Figure 15. The same as Figure 1, but for a random subhalo from our catalog at $z = 1.5$.

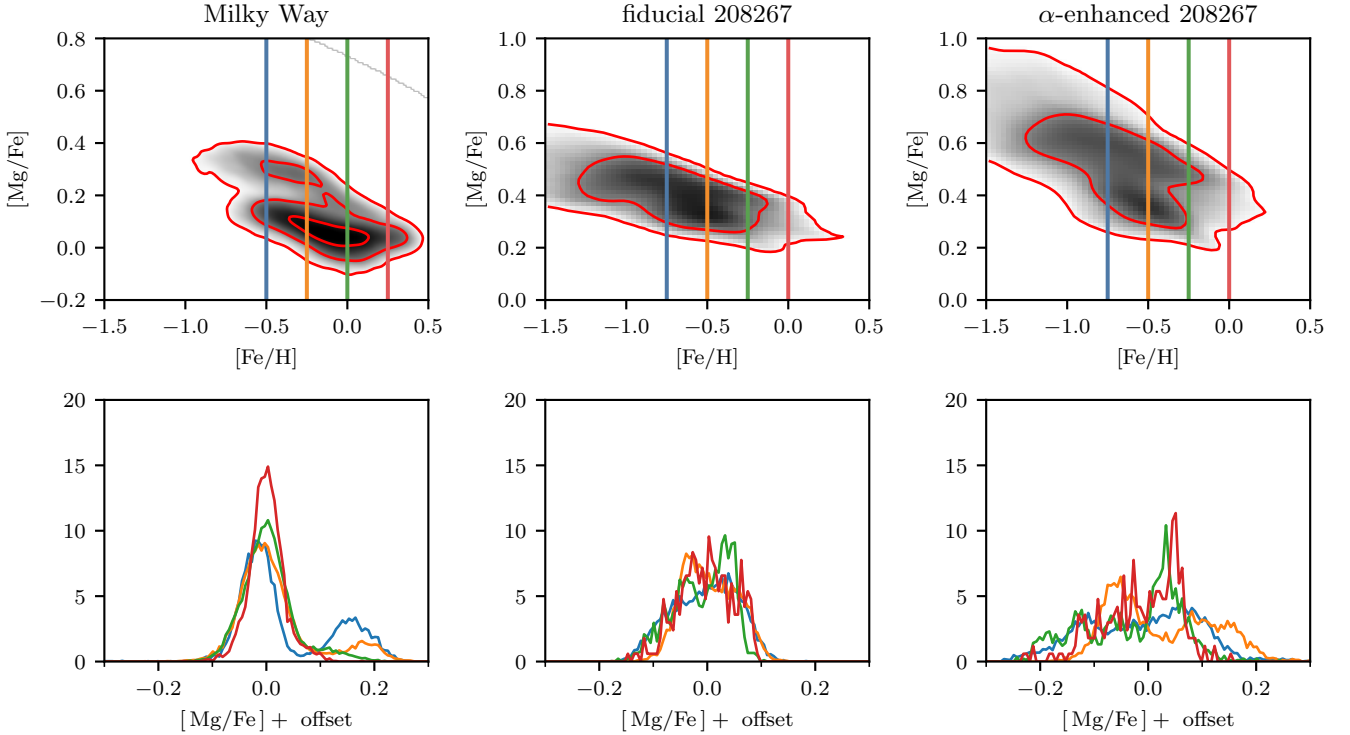


Figure 16. The same as Figure 1, but for a random subhalo from our catalog at $z = 1.5$.

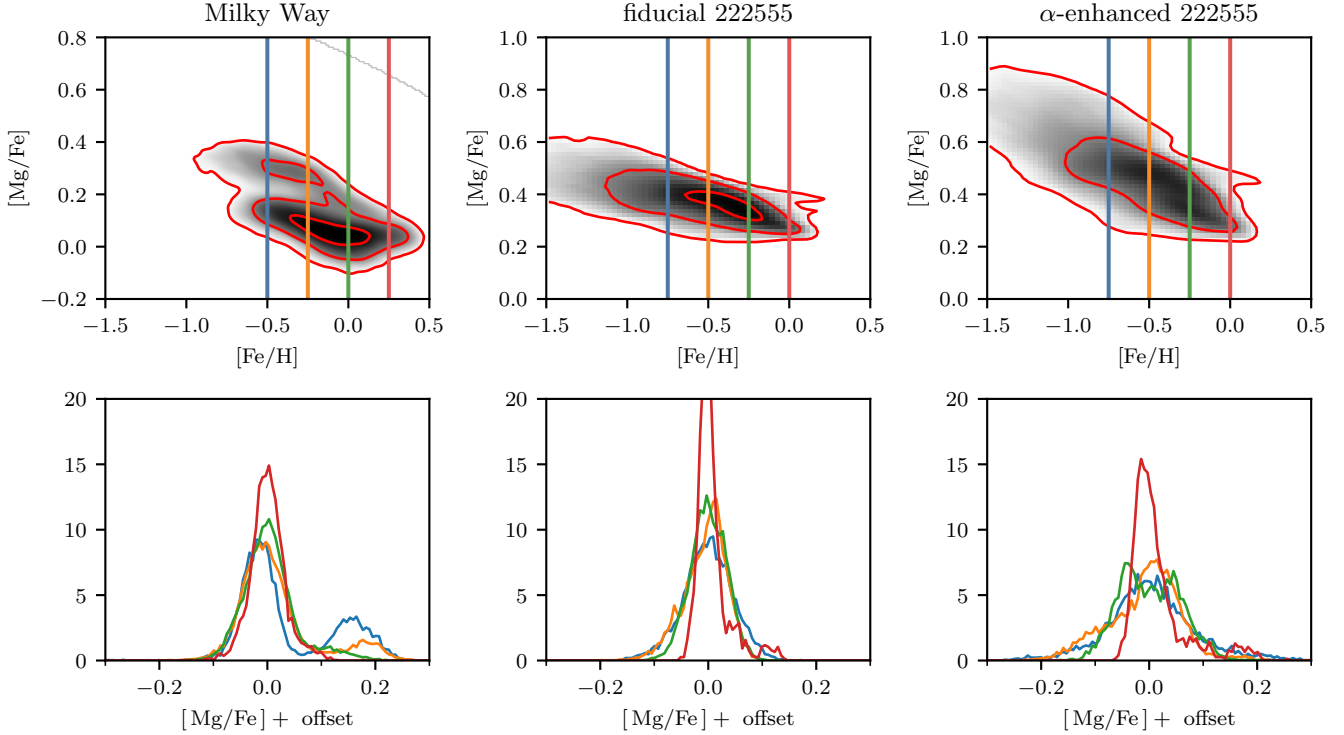


Figure 17. The same as Figure 1, but for a random subhalo from our catalog at $z = 1.5$.

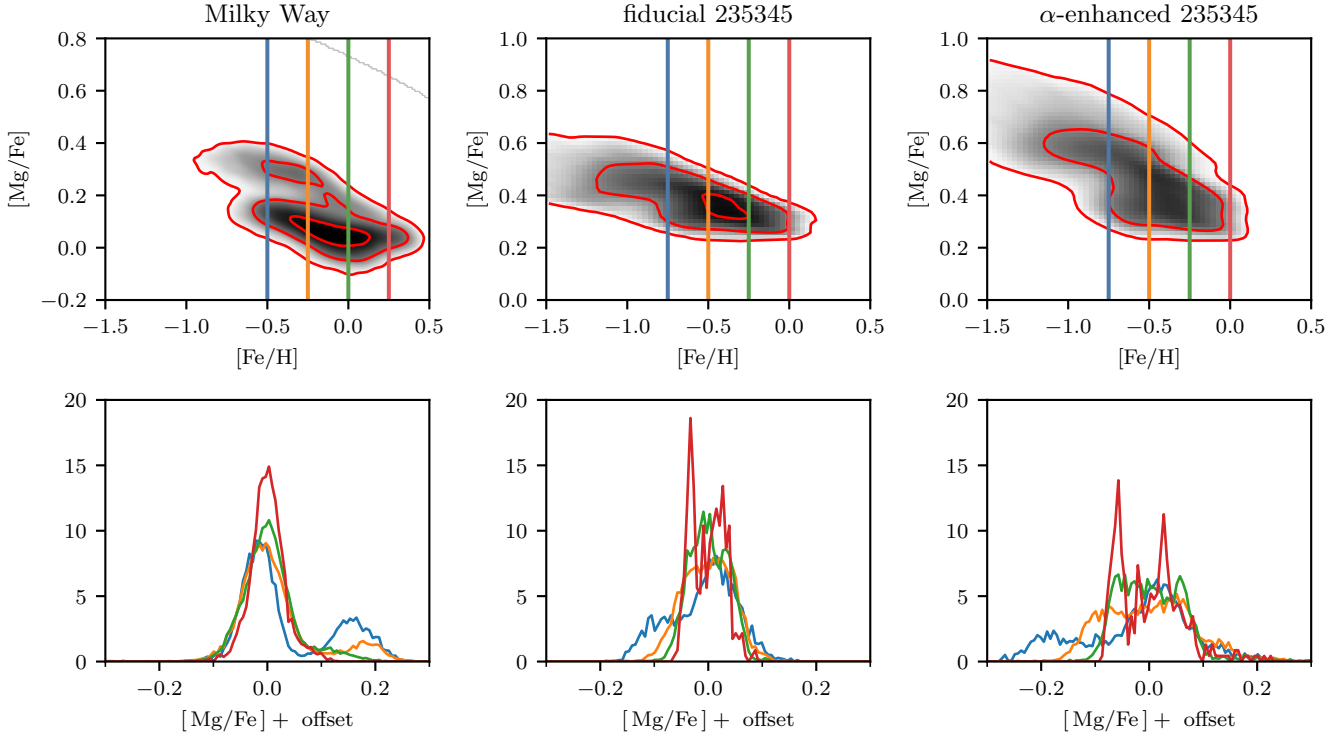


Figure 18. The same as Figure 1, but for a random subhalo from our catalog at $z = 1.5$.

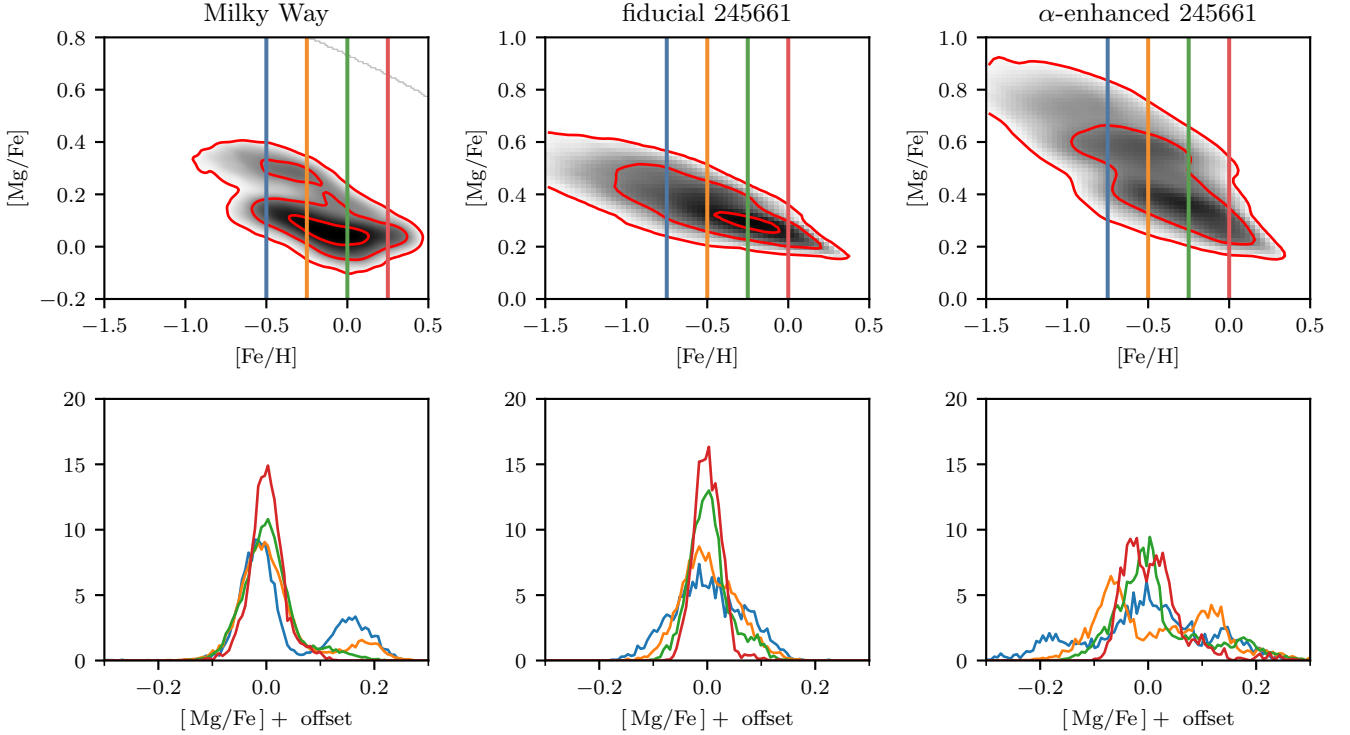


Figure 19. The same as Figure 1, but for a random subhalo from our catalog at $z = 1.5$.

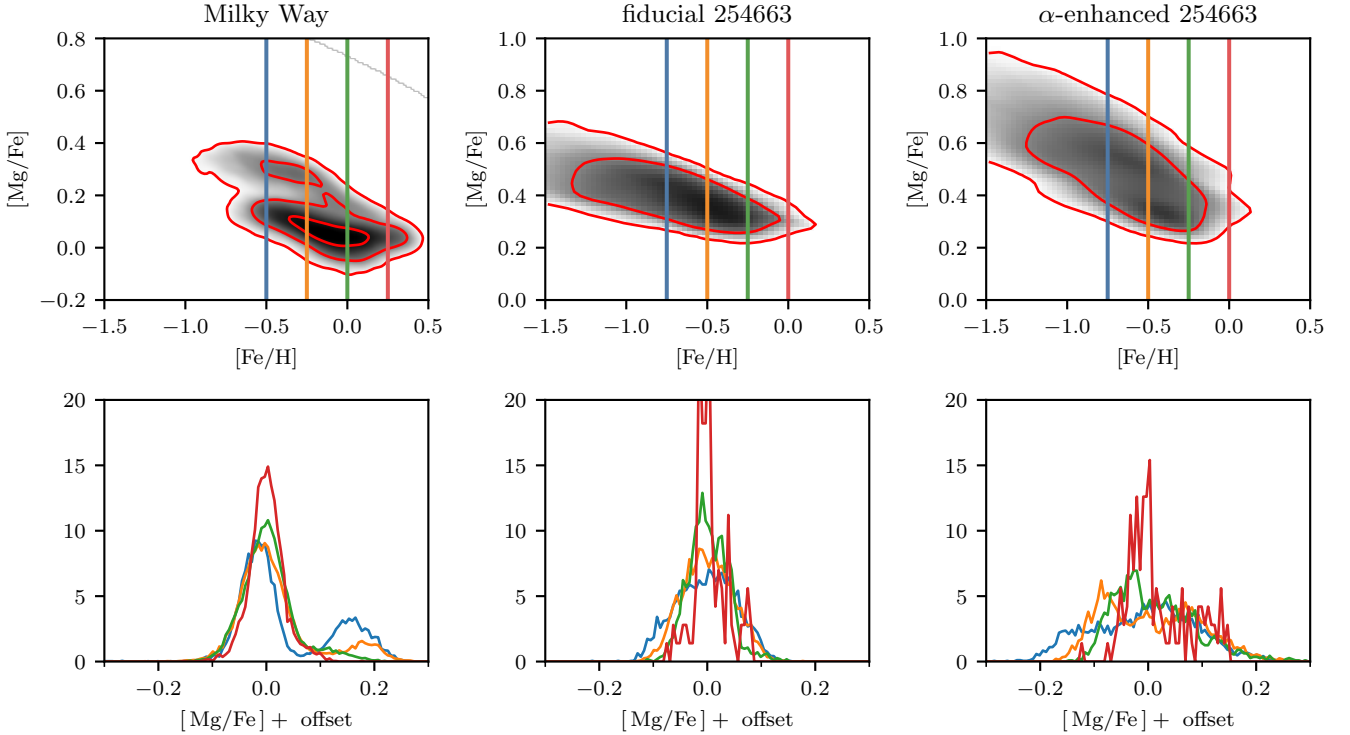


Figure 20. The same as Figure 1, but for a random subhalo from our catalog at $z = 1.5$.

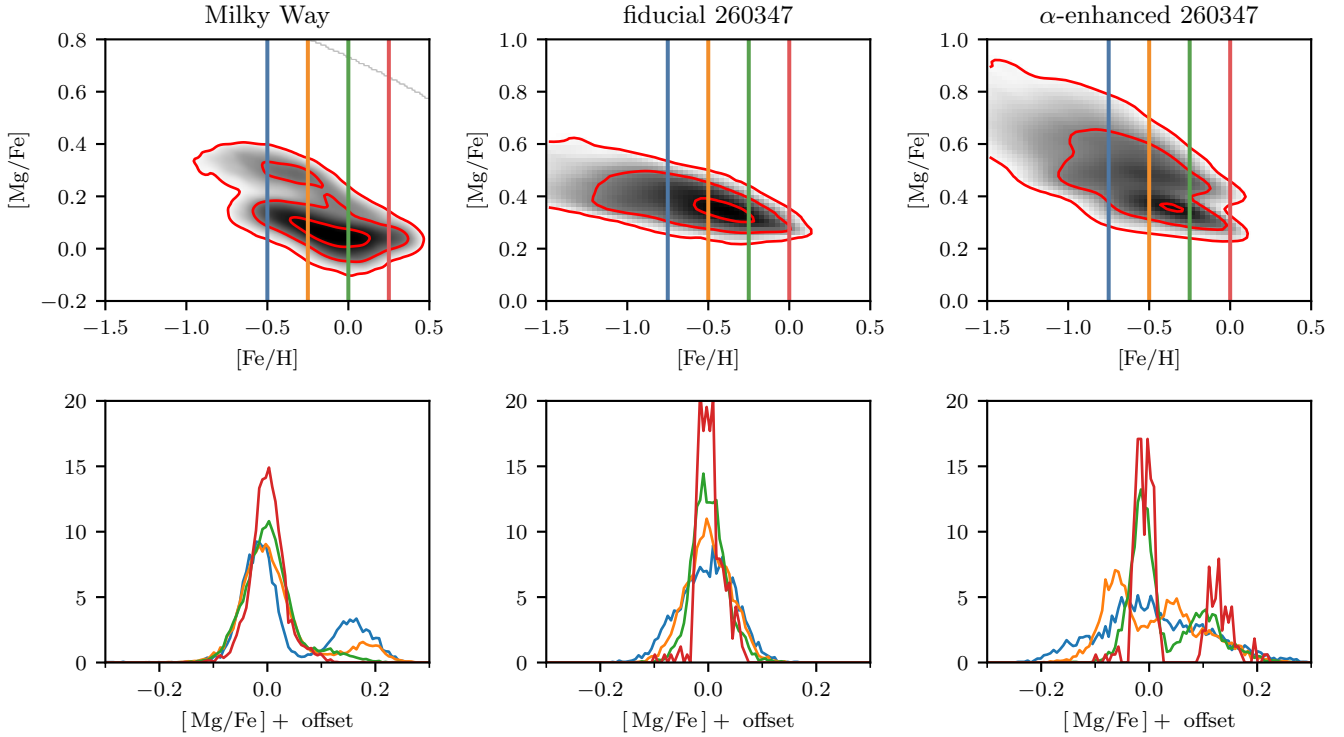


Figure 21. The same as Figure 1, but for a random subhalo from our catalog at $z = 1.5$.

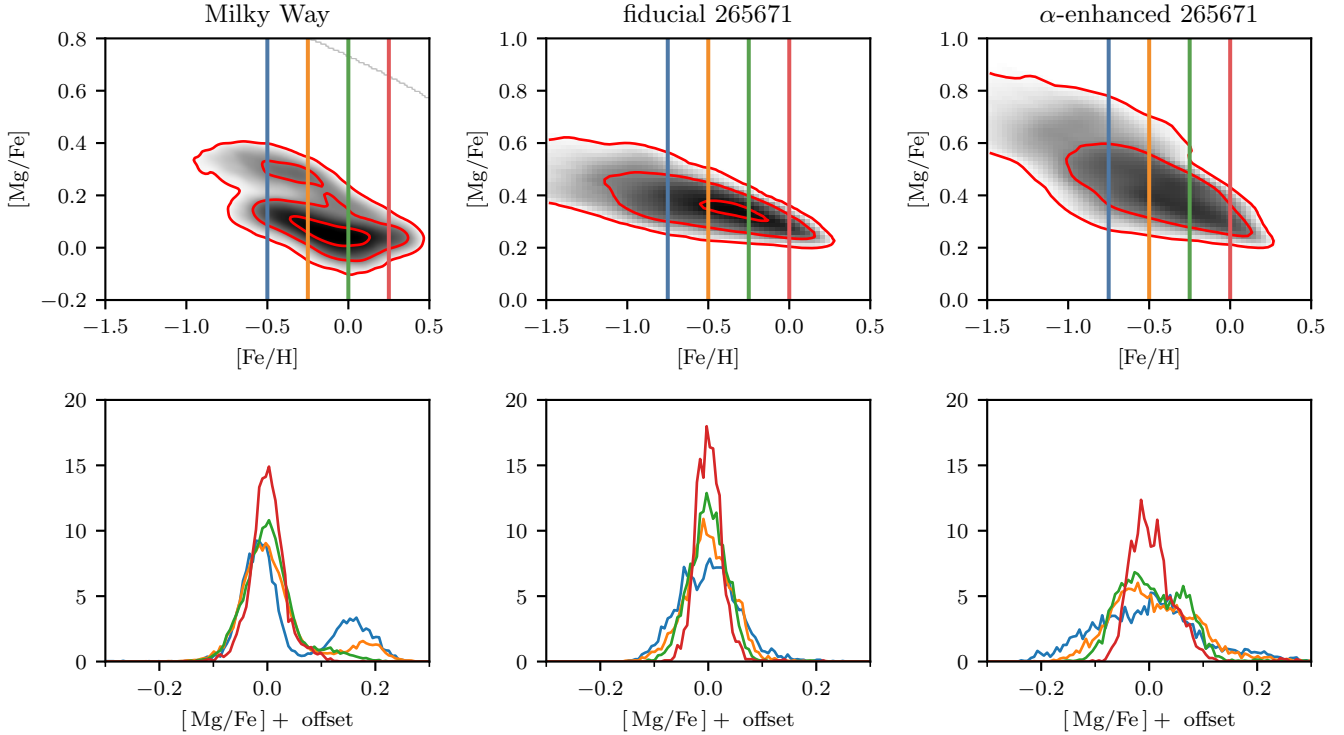


Figure 22. The same as Figure 1, but for a random subhalo from our catalog at $z = 1.5$.

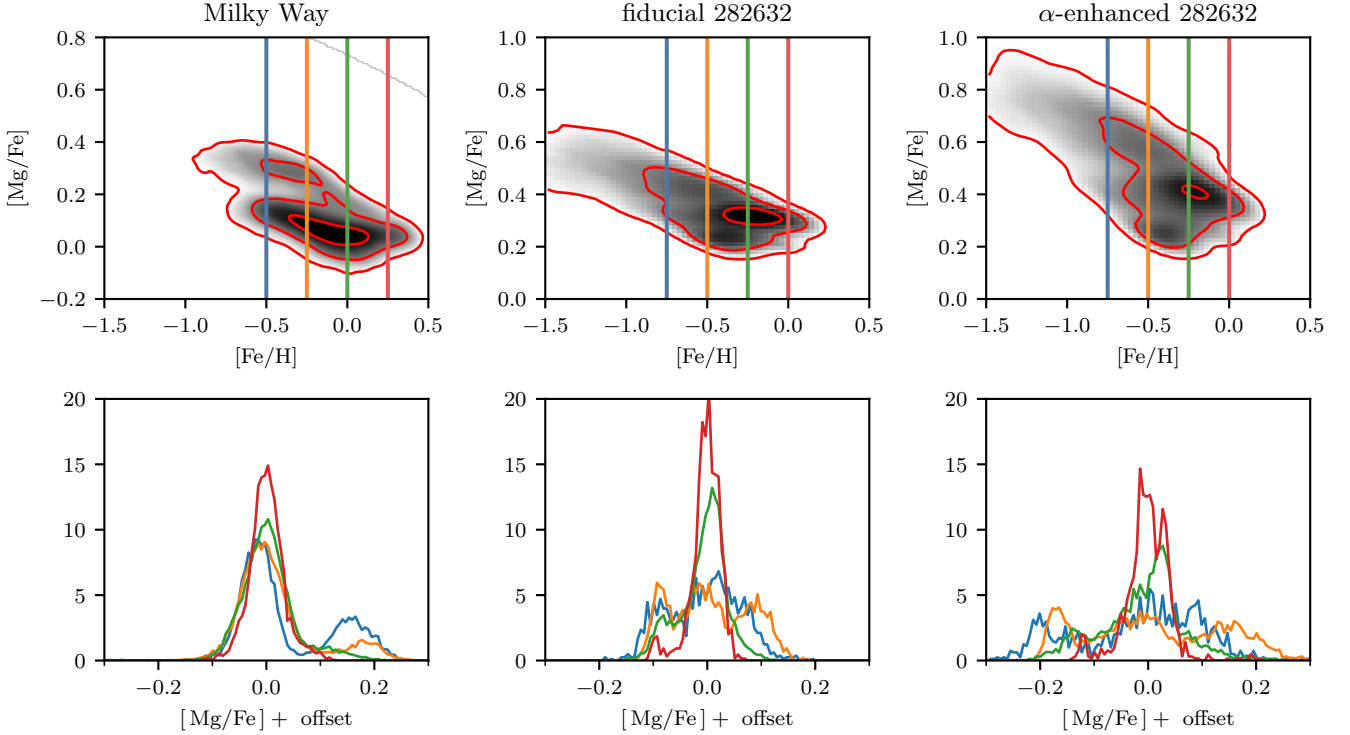


Figure 23. The same as Figure 1, but for a random subhalo from our catalog at $z = 1.5$.

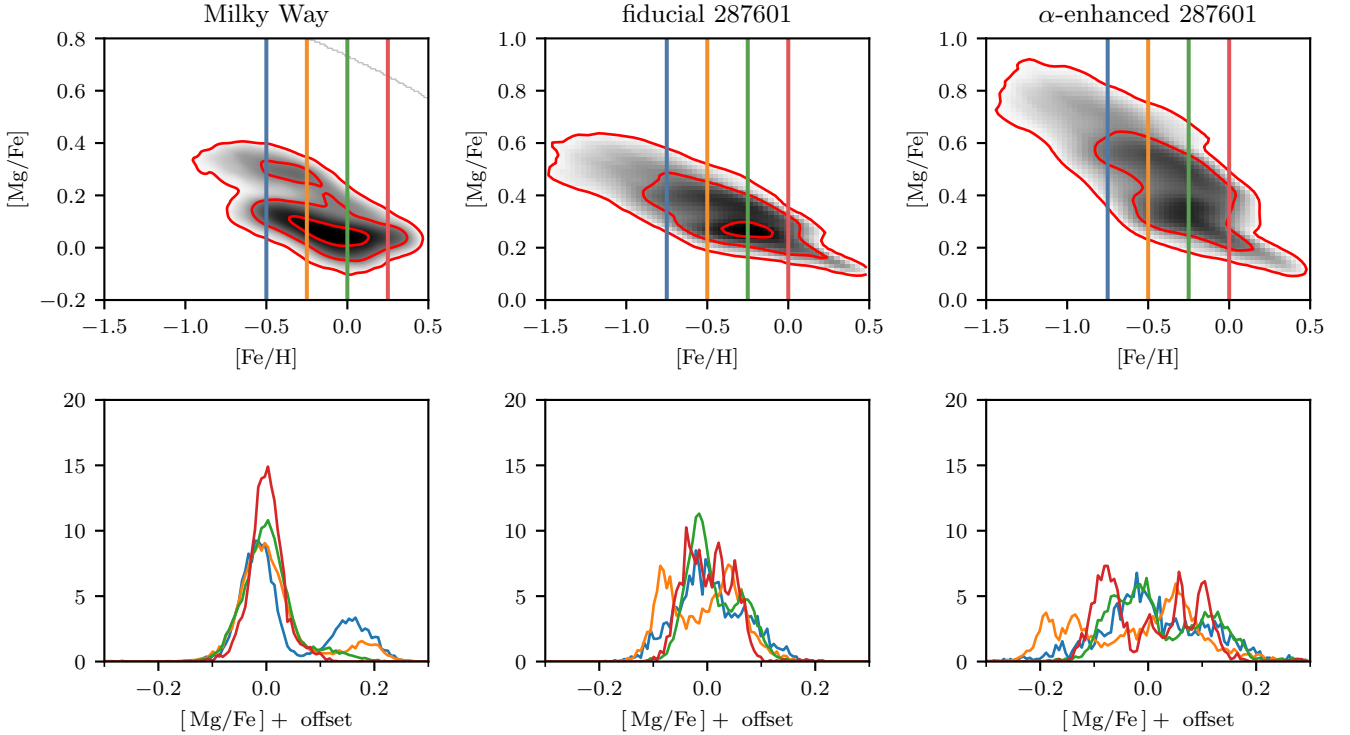


Figure 24. The same as Figure 1, but for a random subhalo from our catalog at $z = 1.5$.

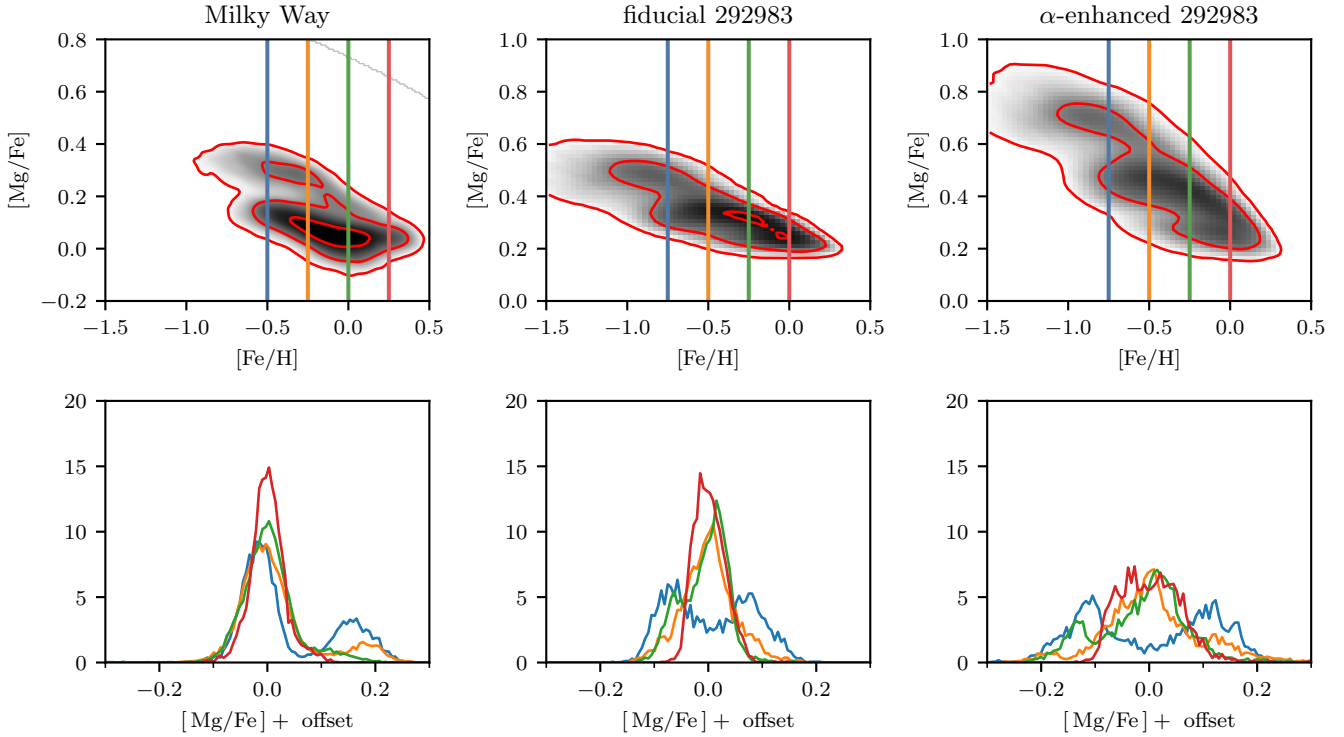


Figure 25. The same as Figure 1, but for a random subhalo from our catalog at $z = 1.5$.